Journal of Asian Earth Sciences: X 9 (2023) 100138

Contents lists available at ScienceDirect

Journal of Asian Earth Sciences: X

journal homepage: www.sciencedirect.com/journal/journal-of-asian-earth-sciences-x

Mid-Norian to Hettangian record and time-specific oolites during the end-Triassic Mass Extinction at Wadi Milaha, Musandam Peninsula, United Arab Emirates

Ingrid Urban [a,*], Isaline Demangel [a], Leopold Krystyn [b], Mikael Calner [a], Zsófia Kovács [a,c], Gerit Gradwohl [c], Simon Lernpeiss [c], Florian Maurer [d], Sylvain Richoz [a]

[a] Department of Geology, Lund University, Lund, Sweden
[b] Department of Palaeontology, University of Vienna, Vienna, Austria Institute of Earth Sciences, Austria
[c] University of Graz, NAWI Graz Geocenter, Graz, Austria
[d] TotalEnergies, France

ARTICLE INFO

Keywords:
Norian-Rhaetian Boundary
Triassic-Jurassic Boundary
Arabian Platform
Chemostratigraphy
Ooids
Modal analysis

ABSTRACT

The end-Triassic Mass Extinction (ETME) is generally regarded as a consequence of the environmental changes associated with the emplacement of the Central Atlantic Magmatic Province (CAMP) and ranks among the 'big five' mass extinctions in Earth history. A notable feature of the ETME is a halt in marine carbonate deposition followed by the formation of unusual facies such as carbonate cement fans and oolites in the early aftermath of the event. The ETME time interval has been well studied over the last few decades, in contrast to a few minor extinction events that preceded it, among them the extinctions associated with the Norian-Rhaetian boundary (NRB). This study provides new insights into these extinction events with complete mid-Norian to Hettangian $\delta^{18}O_{carb}$ and $\delta^{13}C_{carb}$ record from a key section at Wadi Milaha (Ras Al Khaimah Emirate, United Arab Emirates). Ooids are important proxies for palaeoenvironmental reconstruction. The post ETME oolite horizon is documented providing morphological classification as well as a detailed modal analysis of rock components and different types of coated grains. Through a multi-technique approach, we argue for the stability of the carbon cycle across the NRB extinction event and the existence of a hiatus at the TJB (Triassic-Jurassic Boundary) in Wadi Milaha. Our new morphological classification of post-extinction ooids is compatible with a major role for seawater geochemistry with respect to sedimentological processes, by example in the peculiar way ooids diversify and alternate with other kinds of coated grains.

1. Introduction

During the Phanerozoic, mass extinction events repeatedly altered established ecosystem equilibria and reorganized them in completely different ways (Bambach et al., 2002). Global geochemical perturbations are associated with these events, both in the terrestrial and marine realms (Benton, 1995). Among the five major mass extinctions, the end-Triassic Mass Extinction (ETME, 201 Ma ago, Wotzlaw et al., 2014) occurs after several upheavals of different magnitude reported at the Carnian-Norian boundary (e.g., Brusatte et al., 2008; Onoue et al., 2016; Dal Corso et al., 2020), the lower-middle Norian boundary (Lacian-Alaunian) (e.g., McRoberts and Newton, 1995; Sun et al., 2020), and the Norian-Rhaetian Boundary (NRB; McRoberts et al., 2008; Krystyn et al., 2007a, 2007b; Richoz et al., 2012; Rigo et al., 2020). The extinction associated with the NRB affected for example the marine faunas, although it preserved organisms such as scleractinian corals and coccolithophorids (Falkowski et al., 2004; Kiessling, 2010; Demangel et al., 2020). These smaller, late Triassic events are still poorly studied in comparison to the ETME time interval. They occurred in an ice-free time period with high atmospheric pCO_2 (Price, 1999) affected by large-scale tectonic re-organizations, such as the opening of the central Atlantic (Marzoli et al., 1999) and the closure of the Palaeotethys leading to the Cimmerian orogeny (Berra and Angiolini, 2014; Onoue et al., 2018, Kovács et al., 2020).

During the latest Rhaetian, the global carbon cycle record three major perturbations, corresponding to negative Carbon Isotope

* Corresponding author at: Department of Geology, Lund University, Sölvegatan 12, 223 62 Lund, Sweden.
E-mail address: ingrid.urban@geol.lu.se (I. Urban).

https://doi.org/10.1016/j.jaesx.2023.100138
Received 19 October 2022; Received in revised form 10 January 2023; Accepted 12 January 2023
Available online 20 January 2023

Excursions (CIE), due to an input of isotopically light carbon (e.g., Lindström et al., 2012, 2017, 2021; Dal Corso et al., 2014; Marzoli et al., 2018) and a 3–4 °C increase in Sea Surface Temperature (SST) associated with a global warming (McElwain et al., 1999; Knobbe and Schaller, 2018). These perturbations are related to the volcanism linked to the Central Atlantic Magmatic Province (CAMP; Marzoli et al., 1999). This province is characterized by a sub-volcanic phase starting 150 ± 38 ky before the actual basaltic emplacement, while the igneous intrusions are dated the same age as the ETME (201.564 ± 0.015 Ma) (Davies et al., 2017). The metamorphic aureoles, formed by sills emplaced during the sub-volcanic phase, released the thermogenic carbon seen as the main contribution to the negative CIEs (Heimdal et al., 2020; Lindström et al., 2021, Kaiho et al., 2022). An acidification event during the ETME time interval has been proposed as a response to the massive and rapid emplacement of CAMP (Hautmann, 2004; Hautmann et al., 2008; Greene et al., 2012a; Kovács et al., 2022). Indeed, during the ETME, unbuffered or acid-sensitive marine organisms proved to be the most affected by extinction (Knoll et al., 2007; Hautmann et al., 2008; Kiessling, 2010; Clapham and Payne, 2011). Carbonate-poor marls or shales and the absence of reefal biota across the ETME time interval were interpreted as a manifestation of a lapse in carbonate deposition (Hautmann, 2004; Hillebrandt et al., 2013; Kiessling et al., 2007). In contrast, increased spontaneous precipitation of calcite is reported in strata formed in the early aftermath of the extinction event, such as unusual millimetric botryoidal aragonitic fans in British Columbia (Greene et al., 2012b), and anomalously thick oolitic units in different locations around the Tethys, e.g., present United Arab Emirates (Al-Suwaidi et al., 2016; Hönig et al., 2017; Ge et al. (2018, 2019)), Austria (Felber et al., 2015) and Italy (Galli et al., 2007; Bachan et al., 2012). Such unusual precipitation has been described also from the early aftermath of the end-Permian Mass Extinction (EPME; Groves and Calner, 2004; Richoz et al., 2010; Li et al., 2013, 2015).

Ooids are known to be good palaeoclimatic and palaeoceanographic proxies for palaeoenvironmental reconstruction (Kump and Hine, 1986; Opdyke and Wilkinson, 1990; Heydari and Moore, 1994; Li et al., 2017). Their cortices may preserve the original physico-chemical signature of the environments where they formed, both marine and terrestrial (Flügel, 2010). Nowadays, ooids precipitation is restricted to the tropical warm pools (Li et al., 2019) and Bahamas oolitic shoals are well renowned sites of formation (Diaz and Eberli, 2019). Ooid distribution started from the late Archean (Sumner and Grotzinger, 1993) and are recorded from most time periods until present (Simone, 1980). Marine ooids usually form along the margins of carbonate platforms under specific physico-chemical conditions (Duguid et al., 2010). Their formation needs 1) the presence of a potential nucleus (a mineral crystal, a fossil fragment, a fecal pellet, a rock fragment); 2) supersaturated water with respect to $CaCO_3$ and 3) an agitated environment allowing frequent refreshing and degassing of CO_2. Ooids accretion follows a complex process, which has been explained through various models, e.g., abiotic growing in the water column with periodic resting stages (Davies et al., 1978). For larger grains, the precipitation of fringing cement in the ooids cortex was suggested to occur within dune sediment (Anderson et al., 2020). An open question in ooid research is the role of microbial films during formation or post-formation stages. Microbes can promote $CaCO_3$ precipitation in different ways (Dupraz et al., 2009) and a series of studies, both on fossil and recent ooids have investigated different aspects of biologically influenced or biologically induced mineralization in ooids (e.g., Gerdes et al., 1994; Folk and Lynch, 2001; Diaz et al. (2014, 2017); Li et al., 2017; Batchelor et al., 2018). Despite these evidences, ooids biotic origin is still debated and other authors considered them only as a product of chemical and physical processes (e. g. Rankey and Reeder, 2009; Duguid et al., 2010; Trower et al., 2018).

Wadi Milaha (Ras Al Khaimah Emirate, United Arab Emirates) is one of the key sections in the Arabic peninsula documenting the accretion of post-ETME ooids in an equatorial carbonate shallow water platform (Al-Suwaidi et al., 2016; Hönig et al., 2017; Ge et al. (2018, 2019)). Ge et al. (2018, 2019) described the sedimentology and chemostratigraphy ($\delta^{13}C_{carb}$, $\delta^{13}C_{org}$, $\delta^{18}O_{carb}$ and Sr concentrations) in Wadi Milaha section (Ghalilah Formation), with a specific focus on ooids distribution in the early aftermath of the TJB crisis. In this study, we expand the stratigraphic and sedimentologic description and the $\delta^{18}O_{carb}$ and $\delta^{13}C_{carb}$ records from the mid-Norian to the Hettangian. Moreover, we propose a new morphological classification of the ooids formed in the immediate aftermath of the ETME, supported by light microscopy and Field Emission-Scanning Electron Microscopy (FE-SEM) investigations. We implement the modal analysis of thin sections presented by Ge et al. (2018) with point counting of the different types of ooids. To address lateral stratigraphical and sedimentological variations in the proximity of the TJB, we study two coeval profiles (named WM2 and WM3 and spanning ca. 7 m. across the ETME) in addition to the main mid-Norian-Hettangian profile (named WM). Our multi-technique approach was chosen to understand factors that favoured ooid deposition and their connection to the environmental stress during a mass extinction time interval.

2. Geological setting

The three studied sections are located in the Arab Emirate of Ras Al Khaimah (Fig. 1A), in the western part of the Musandam Peninsula (Maurer et al., 2008; Fig. 1A). The Musandam Peninsula is part of a mountain chain that exposes a 3-km-thick succession of shallow water carbonates ranging from Permian to Cretaceous (Maurer et al., 2009). This mountain chain is the prolongation of the Oman Mountains towards northwest (Maurer et al., 2009). During the Upper Triassic and Lower Jurassic, the Arabian shelf was at the palaeoequator, bordered by the Arabian shield in the southwest and the Tethys Ocean in the northeast (Maurer et al., 2008, Richoz et al., 2014, Fig. 1B). The studied succession was deposited along the eastern margin of the Arabian shelf, on an equatorial shallow water carbonate platform (Glennie et al., 1974; Ziegler, 2001; Richoz et al., 2014). The northern part of the platform was characterized by more open-marine conditions, whereas terrigenous input came from land areas in the south or south-west (Ziegler, 2001). The eastern margin of the Arabian Plate was active in the Late Cretaceous when the Semail Ophiolite was obducted on the plate (Glennie et al., 1974; Glennie, 2005) and in the Late Oligocene-early Miocene, when the Musandam and Oman Mountains were raised in connection to the Zagros orogeny (Searle et al., 2014). Sections in the area are generally well exposed and moderately overprinted by diagenesis (Searle, 1988). The main studied section, Wadi Milaha (WM), is a composite log starting from the Upper Triassic at Wadi Bih (Base N 25°46′09.5″ E 56° 2′27.2″; top N 25°45′50.8″ E 56° 2′22.1″) for the first 230 m until a fault above two marker sandstone beds. Above these marker beds, the overlying 234 m of the log continue at the neighbouring Wadi Milaha (Base N 25°45′39.5″ E 56° 2′58.4″; top N 25°45′30.6″ E 56° 2′17.7″) continuously until the Middle Jurassic. The part of the section studied in the Wadi Bih area is composed of the Norian Milaha Formation (Maurer et al., 2008; Clarkson et al., 2013) and the main part of the section at Wadi Milaha comprises the upper part of the Milaha Formation and the Norian to Hettangian Ghalilah Formation (Fig. 1C). The isochronous sections Wadi Milaha 2 (WM2) and Wadi Milaha 3 (WM3) are located at N 25° 45.442′ E 056° 02.325′ and N 25° 45.393′ E 056° 02.452′, respectively. The Wadi Milaha section is located 120 m West of WM2 which is 260 m West of WM3. The WM section is ca. 980 m West of the reference section of Ge et al. (2018, 2019). Wadi Milaha 2 and Wadi Milaha 3 span only the end-Triassic extinction interval in the Ghalilah Formation.

2.1. Chronostratigraphic framework of the Wadi Milaha section.

The Ghail Formation, a 500-m-thick succession of peritidal dolostones, underlie the Milaha Formation. It was dated as Olenekian to Ladinian (-Carnian?) based on foraminifera species (Maurer et al.,

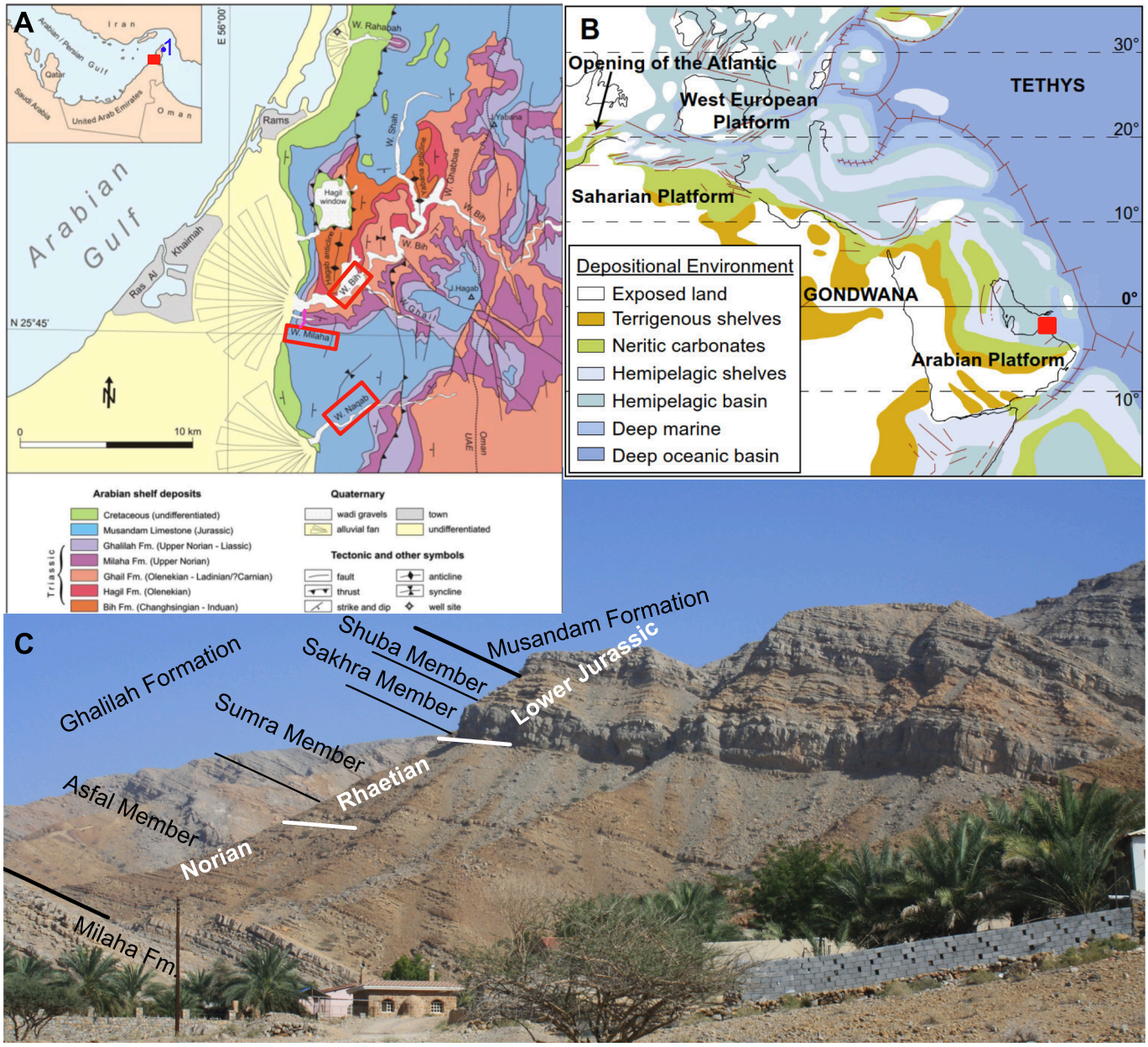

Fig. 1. A. Geological map of the western Musandam Peninsula (Ras Al Khaimah Emirate) with the location of the measured section in pink (dashed line); Wadi Bih, Wadi Milaha and Wadi Naqab, cited in text, in red rectangle. Insert map (top-left): Geographical location of Musandam Peninsula, with 1 the cited Dawhat Qabal section. Modified from Maurer et al. (2008), Biehler et al. (1975) and Searle (1988). B. Palaeogeographical location of Musandam Peninsula (red square) and the Arabian shelf in the Early Jurassic. Hönig et al. (2017), modified from Pierre (2006) ; after Thierry and Barrier (2000). C. Panorama of the studied section in Wadi Milaha locality, with indication of the periods as well as boundaries between formations and members highlighted. (For interpretation of the references to colour in this figure legend, the reader is referred to the web version of this article.)

2008). The Milaha Formation, a succession of peritidal carbonates (limestone and dolostone), was dated as mid to upper Norian (Fig. 1C, 2), based on macrofauna –especially megalontids, typical of the Norian (Hudson, 1960) and foraminifera species (Maurer et al., 2008). Among several Late Triassic species, the late Norian/Rhaetian index foraminifer *Triasina hantkeni* Majzon, was found 21 m above the base of the formation as well as 50 m below the top of the formation (Maurer et al., 2008). A conodont-controlled late Norian age for *T. hantkeni* is known from the Northern Calcareous Alps (Reijmer et al., 1991). However, its supposed forerunner, *T. oberhauseri*, has been described from the lower Norian Dachstein Limestone of Austria. A middle Norian age for *T. hantkeni* and by consequence for the Wadi Milaha Formation can thus not be excluded. This age attribution indicates a large hiatus spanning the Carnian and Lower Norian between Ghail and Milaha formations.

The Ghalilah Formation is a mixed carbonate-siliciclastic unit, subdivided into four members: the Asfal, Sumra, Sakhra and Shuba members (Fig. 1C, 2, 3, 4) (Maurer et al., 2008 after Hudson, 1960). The age of the Ghalilah Formation (Fig. 2) has been determined through micro- and macrofossil assemblages (Maurer et al., 2008, this study). Late Triassic foraminifera such as *Aulotortus* ex gr. *sinuosus*, *Aulotortus friedli*, *Auloconus permodiscoides* (Oberhauser), *Agathammina austroalpina* and lagenids were reported, although the classical index fossil for Norian-Rhaetian *Triasina hantkeni* is missing (Maurer et al., 2008). The finding of one ceratitid ammonoid *Neotibetites weteringi* (BOEHM), 22 m above the base of the Asfal Member (Maurer et al., 2008) suggests a late Norian (Sevatian) age for these strata (Bhargava et al., 2004). The top of

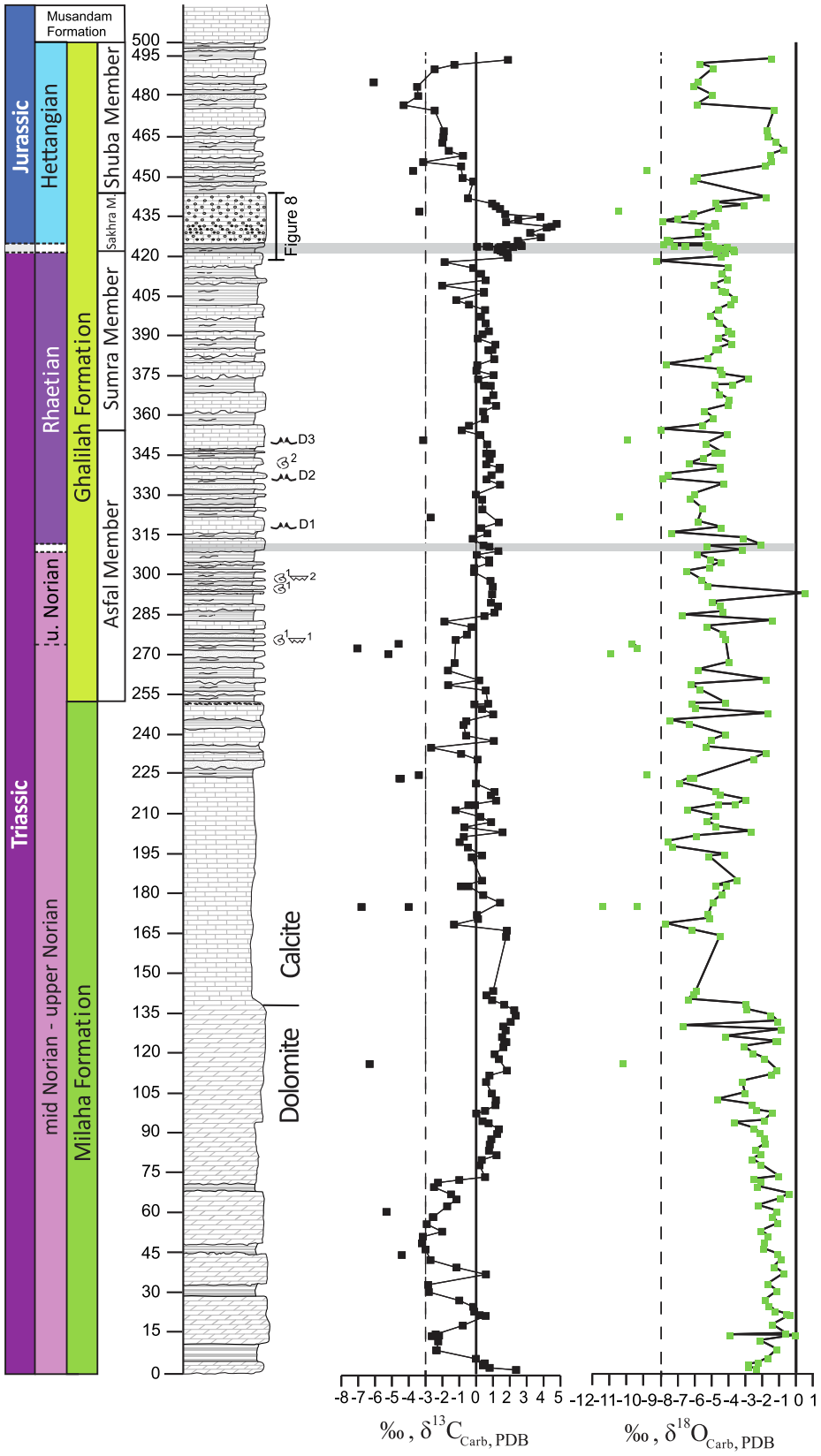

Fig. 2. Simplified litho- and chronostratigraphy of the Wadi Milaha section with $\delta^{13}C_{carb}$ and $\delta^{18}O_{carb}$ curves. The dashed lines at −3 ‰ and −8 ‰ respectively mark the threshold for outliers. D1, D2 and D3 mark the *Dicerocardium* beds 1, 2, and 3. Ammonite 1; *Neotibetites weteringi*; ammonite 2: *Arcestes* sp., conodont 1: *Epigondolella bidentata,* conodont 2: *Misikella hernsteini* and *Parvigondolella andrusovi.* A detailed profile is avaliable in the supplementary material.

the Asfal Member was assigned until now to the Norian based on the occurrence of the hydrozoan *Heterastridium* (Marcoux et al., 1993; Flügel, 2010 and related references) at two different levels (Maurer et al., 2008). However, new conodont and ammonoid findings (this study, Fig. 5) allow us to place the Norian-Rhaetian boundary in the interval 309 to 312 m (see results below) and thus assign a Rhaetian age for the top of Asfal Member and the Sumra Member. Whereas the Asfal Member, due to its pelagic fauna of cephalopods and conodonts, is well datable, the less open marine Sumra Member, which contains typical Rhaetian fauna (bivalve, coral, calcareous sponges, foraminifera), lacks biostratigraphically relevant organisms and allows no high-resolution subdivision. The absence of micro- and macrofauna in the Sakhra Member and in the lower part of the Shuba Member was interpreted as a consequence of the ETME by Maurer et al. (2008), who suggested the TJB to be at the base of the Sakhra Member, immediately on top of coral framestones of the Sumra Member. We follow this interpretation, although, this position is still under debate (de Matos, 1997; Hönig et al., 2017), see discussion later in subsection 5.1.3.

3. Materials and methods

After detail investigations in the field, a total of 357 representative rock samples were collected for further analysis and thin section preparation. For Wadi Bih part of the section, 112 hand samples were collected (WB1-111), while 205 hand samples (WM 1-WM 104; WM 150–209; WMG 1–21; WMG 92–100) were collected for the main Wadi Milaha section (Fig. S1). Twenty-two samples were collected from Wadi Milaha 2 and 18 from Wadi Milaha 3.

A standard, 30 μm thick, uncovered thin section (28 × 48 mm) was cut from each sample and described in detail with an Olympus BX50 petrographic optical microscope, equipped with a digital camera (Olympus SC50). Lithologies were classified according to the Dunham classification (Dunham, 1962) as revised by Embry and Klovan (1971) and Wright (1992). Standard microfacies (SMF) were described according to Wilson (1975) and Flügel (2010). Petrographic and textural features of the rock, such as bioclast type and content, grain size, roundness and sorting were studied, as well as early (micritization, replacement and early cementation) and late (e.g., presence of veins and stylolites) diagenetic features. Of particular importance was the study of the arrangement of crystals in the cortex laminae of ooids for a morphological classification of these grains. Both parallel and crossed nicols configuration were applied. For a quantitative evaluation of the distribution of different types of ooids and coated grains, six thin sections from the Wadi Milaha section and two each from the auxiliary sections (Wadi Milaha 2 and 3) were scanned with a Canon slide scanner at 4000 dpi and then point-counted with JMicroVision® software (Roduit, 2022). A random grid was used with spots having a default size of ten pixels (cf. Roduit, 2007). The number of points counted per section was 300 (cf. Galehouse, 1971). This number represents a minimum reference value to be considered statistically significant, as the percentage of each rock component in our thin sections becomes stable. To investigate further microstructures related to diagenetic processes and potential microbial interaction, ooids from twelve selected samples were imaged at the Department of Geology at Lund University with a variable pressure Tescan Mira3 High Resolution Schottky FE-SEM equipped with an Oxford EDS detector, at 5 kV. Samples were prepared as small rock chips (5X5X8 mm) with a fresh broken surface, then sputter coated with platinum/palladium (Cressington sputter coater 108 auto, 20 mA, 20 s).

The calcareous nannofossils content was analysed using scanning electron microscopy. Eight samples were prepared following the method of Demangel et al. (2020, 2021). Blocks with a surface of 1 cm^2 were cut into the fresh sample surface perpendicular to the bedding plane to reduce the effect of sample heterogeneity (Chayes, 1954). The surfaces to be analysed were polished with HV 600 and 1200 diamonds discs using deionized water then etched for 15 s in 0.1 % HCl solution and cleaned with distilled water. The samples were dried overnight at 50 °C, coated with a 1 nm thin layer of Pt/Pd and observed in the FE-SEM as described above.

Measurements for stable isotopes analyses ($\delta^{13}C_{carb}$ and $\delta^{18}O_{carb}$) were conducted on different rock components (matrix, ooids and carbonate cement). A total of 103 isotope samples from the part of the section in Wadi Bih were selected at an average stratigraphic spacing of 2,19 m. An additional 199 isotope samples were selected for the Wadi Milaha area. All rock components were drilled with a diamond bit, avoiding visible fossils, veins or fractures. The Wadi Bih samples were reacted with 100% phosphoric acid at 70 °C in a ThermoFinnigan Kiel II autosampler connected online to a Delta V Plus mass spectrometer at the Institute for Earth Sciences, University of Graz (Austria). They were dissolved in acid for three (calcite) to ten minutes (dolomite). All values were then reported as per mil relative to V-PDB (Vienna- Pee Dee Belemnite) international standard. Standard deviations (1 σ) of measurements from the in-house and NBS19 standards were less than ± 0,15 ‰ and ± 0,25 ‰ for $\delta^{13}C$ and $\delta^{18}O$, respectively. The samples from the Wadi Milaha section were instead processed at GeoZentrum Nordbayern, University of Erlangen-Nuremberg (Germany) with a ThermoFinnigan Delta V Plus mass spectrometer. The powders were reacted with 100% phosphoric acid at 70 °C in a Gasbench II autosampler connected online to the mass spectrometer. All values are then reported as per mil relative to V-PDB by assigning $\delta^{13}C$ values of + 1.95‰ to NBS19 and − 47.3‰ to IAEA-CO9 and $\delta^{18}O$ values of − 2.20‰ to NBS19 and − 23.2‰ to NBS18. Reproducibility for $\delta^{13}C$ and $\delta^{18}O$ was ± 0.04 ‰ and ± 0.04 ‰ or 0.05 ‰ (1 σ), respectively. In the case of outliers, they were re-measured and they did not show any relevant deviations.

4. Results

4.1. Lithostratigraphy

The Milaha Formation (Figs. 2, 6) is a Late Triassic succession of peritidal carbonates (limestone and dolostone). Its lower part is composed of grainy dolomite interbedded with up to 1 m-thick marls. These dolomites are grainstones with a rich fossil assemblage, including bivalves, gastropods, Dasycladacean algae and the foraminifer *Aulotortus* sp. (Fig. 6C). Within this unit, from 0 to 67 m, stromatolites often occur (Fig. 6D) and provide useful marker beds. Above, the dolomite transitions to a packstone-grainstone with a recrystallized, sparitic matrix and rich fossil assemblage of Dasycladacean algae, *Tubiphytes* and the foraminifera Duostaminidae, *Aulotortus* ex gr. *sinuosus* and *Hoyenella sinensis* (Fig. 6F). At 138.5 m, there is a sharp change from dolomudstone to lime-mudstone. Crinoids increase in abundance from 159 m and upwards. Thick shelled bivalves of the genus *Dicerocardium* first appear at 167 m and become more abundant within the overlying Ghalilah Formation at 317 m. At 217 m, a bed exceptionally rich in in situ corals and Dasycladacean algae forms a marker bed (Fig. 6E). Above, the amount of siliciclastic beds (quartz and clay) increase. These beds alternate with well bioturbated nodular wackestones and carbonate mudstones. This upper part of the Milaha Formation includes the two yellow sandstone beds (227 to 230 m), which are the marker beds allowing the correlation from Wadi Bih to Wadi Milaha. A 4 m thick carbonate mudstone with large megalodontids, sometime as mould, is covered by a 40 cm conglomerate, which marks the upper boundary of the Milaha Formation at 252 m. This intraformational breccia, which can laterally thicken to a 4 m thick layer, is interpreted as sequence boundary (Fig. 3 A-B).

In Wadi Milaha section, the Asfal Member of the Ghalilah Formation (Fig. 7 A-E) is a 103-m-thick siliciclastic-dominated alternation of dark, red-weathered quartz arenites and marlstones, with subordinate carbonate rudstones and mudstones (Maurer et al., 2008). The bioclastic content includes bivalves, crinoids, gastropods, ammonoids, solitary and branched corals, brachiopods, thick-shelled bivalves of the genus *Dicerocardium*, Chaetitids, hydrozoans of the genus *Heterastridium* and traces of algal mats. The upper part of the member shows three distinct

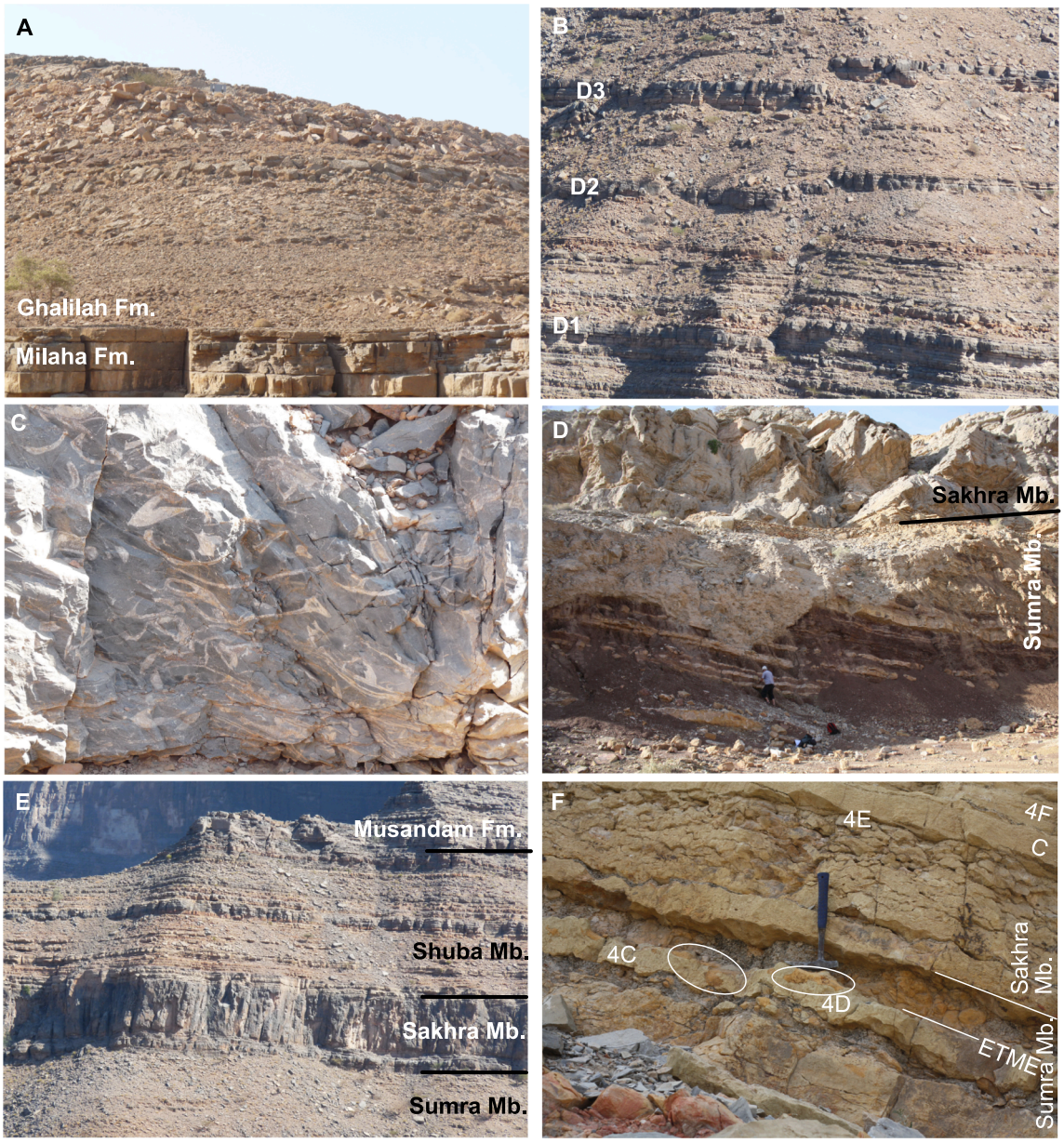

Fig. 3. Field picture of the Wadi Milaha section. A. Transition between the Milaha Formation and the Ghalilah Formation. B. The upper Asfal Member of the Ghalilah Formation with the three *Dicerocardium* marker beds (D1, D2, D3). C. A *Dicerocardium* bed with some megalodonts as well. D. Alternance of limestone and red shales in the top of the Sumra Member, with above the cliff forming Sakhra Member. E. General view of the Sakhra and Shuba members. F. The Sumra-Sakhra boundary with the end-Triassic Mass Extinction (ETME) event. The circles highlight trace of erosion and filling with orange marls just before the extinction levels, the number refers to enlargement in Fig. 4, C represents the first bed with coated grains. (For interpretation of the references to colour in this figure legend, the reader is referred to the web version of this article.)

thick carbonate beds rich in *Dicerocardium* (at 316–322; 336–338 and 349–354 m). These several meters thick limestone beds protrude morphologically and are laterally continuous over tens of kilometres. They can be used as lithostratigraphic marker beds both from morphology and distinct litho- and biofacies. The last of these *Dicerocardium*-rich beds is overlain by 1,5 m thick fossiliferous wackestone, which marks the base of the Sumra Member.

Chronostratigraphically significant fossils confirm an upper Norian age for the lower Asfal Member till below the first *Dicerocardium* bed (316–322 m, Fig. 7E). Indeed, the ammonoid *Neotibetites weteringi* (Boehm) occurs from 274 m to 298 m (samples WM 20, WM 21/22, WM 30, WM 31) and the conodont *Epigondolella bidentata* Mosher (Fig. 5A) occurs at 274 m (WM 20). Conodonts interpreted as late upper Norian further occur between 298 m and 309 m including *Misikella hernsteini* (Mostler) in WM 31, WM 32, WM 37 (Fig. 5 B-D) and *Parvigondolella andrusovi* (Kozur) in WM 37. Conodonts and ammonoid become then rare in Wadi Milaha between the three thick *Dicerocardium* shell beds.

Above, the Sumra Member is 69 m thick, more fossiliferous, but with less pelagic fauna, and clay-rich, but without quartz arenites (Fig. 7F). A detailed description of bivalve and brachiopod taxa as well as of hypercalcified sponges within this member can be found in Hudson and Jefferies (1961) and Senowbari-Daryan and Maurer (2008), respectively. The uppermost 4–5 m of the Sumra Member constitute coral rudstones/floatstones and an alternation of floatstones, packstones, packstones/wackestones and wackestones/mudstones containing corals from the genera *Retiophyllia* and *Thamnasteria* (Maurer et al., 2008), sponges, bivalves, crinoids and echinoids, bryozoans, gastropods and foraminifera (Fig. 3D). As highlighted by Maurer et al. (2015), an

interesting aspect of the Asfal and Sumra members' fauna is the co-presence of species whose type-localities span across the Tethys and the Panthalassa Ocean: foraminifer *Triasina hantkeni* (locus typicus: Dachstein, Northern Calcareous Alps), sponge *Lovcenipora chaetetiformis* (Timor), pectinid bivalve *Indopecten clignetti* (Buru, Indonesia) and alatoform bivalve *Wallowaconchia* (Wallowa Terrane, USA).

The Sumra Member is overlain by the Sakhra Member, which is 19 m thick. The ETME horizon occurs at the transition between the two members (Figs. 2, 3F, 4). The top of organisms-rich floatstone-packstone series is covered with a Fe-Mn crusts overlain by 7 cm black shales, 8 cm of olive-coloured bioclastic limestone with lenses of orange marls and 20–40 cm of orange marls. A characteristic 40 cm bioclastic floatstone (Fig. 4B) with large elements of reworked corals and 4 cm of orange marls with olive limestone lenses follow. The next 20 cm thick bioclastic olive limestone (Fig. 4 C-D) shows laterally trace of erosion with an orange marly filling and some sub-angular clasts of the same limestones, showing little to no transport. We consider the top of this bed as corresponding to the main extinction level. It is overlain by 2 to 10 cm orange marls, whose top represents the Sumra to Sakhra members boundary. The latter starts with two wackestone-packestone to rudstone-grainstone beds, 13 and 40 cm thick respectively. The upper one has laterally the appearance of flaser beds or *in situ* breccia (Fig. 4E). In some places, this in situ breccia can extend downward and encompasses all the extinction interval, affecting Rhaetian corals floatstone as well. The upper surface is irregular and, in some places, shows traces of karstification. Above starts 2 m of bioclastic packstone and grainstone alternation, rich in superficially coated grains, ooids and peloids. Some of the basal beds are cross-stratified. The most common bioclasts are bivalves, gastropods and echinoderms. Around 2 m above the base of the member, there is in some places mass occurrence of two types of not extractable, small (≤1.5 cm), black-coloured thin bivalve shells, which could not be determined even generically. They resemble in part to the lower Hettangian *Liostrea* and *Modiolus* pavements of the English Blue Lias Formation (Mander et al., 2008). The overlying 6 m show great variability in lithology and include grainstones, grainstones/packstones, packstones, packstone/wackestones, wackestones/mudstones and mudstones. The uppermost 9 m are dominated by packstones with intercalated grainstones and cross-stratified grainstones. The Ghalilah Formation ends with the Shuba Member, which is ca. 40–50-m-thick. The first two meters represent peloidal packstones, alternating with marls, overlayed by marlstone, dolomitic mudstone and siltstone, often displaying subaerial desiccation cracks at their top. Macro and microfauna are rare. The overlying Musandam Formation is thicker-bedded, cliff building and starts with an oolitic grainstone, alternating with crinoids packestone, and bioclastic pack- and grainstone.

4.2. Standard microfacies across the ETME interval

4.2.1. Coated grains characterization

Coated grains were characterized in the following categories: a) superficially coated grains (definition modified from Carozzi, 1957), with just one lamina surrounding the nucleus and the thickness of the cortex always less than half of the diameter of the entire grain; b) radial ooids; c) concentric ooids; d) concentric-radial ooids; e) micritic ooids (i.e., with laminae originally made by randomly arranged crystals); f) completely micritized ooids (i.e., ooids that originally belonged to different categories, but their cortices were later completely obliterated by bacteria or endolithic organisms); g) partially micritized ooids (i.e., ooids altered in the same way as completely micritized ooids, but with laminae edges still visible; however, internal crystal arrangement is not detectable).

4.2.2. The main Wadi Milaha section

The sedimentary facies during the extinction interval (ca. at 423–424 m in Fig. S1 detailed log), can be assigned to three different standard microfacies (Figs. 8, 9). First, bioclastic packstone and wackestone with abraded, worn bioclasts. Second, wackestone with whole and fragmented fossils. Third, rudstone and grainstone with prevalent densely packed whole fossils and fragments.

Abundant types of ooids occurs within 1 m above the extinction interval (samples WM 166, 167). The first grains with trace of coating appear in a poorly sorted peloidal grainstone/packstone (sample WM 166). It contains superficially coated grains, possible extraclasts and cortoids, i.e., carbonate grains, such as bioclasts, ooids, lithoclasts or peloids whose periphery exhibits a circumgranular non-laminated micritic rim commonly called a "micrite envelope" (Flügel, 2010). The overlying bed (WM 167) also contains superficially coated grains but in contrast some micritized or partially micritized ooids together with peloids and cortoids, in a moderately sorted grainstone (Fig. 10A). The nuclei of ooids in the sample WM 167 are not well recognizable, but likely made of peloids and bioclastic fragments. In the following samples, superficially coated grains still prevail over ooids, but some small radial and/or micritized ooids appears for the first time (WM 170, 424 m, Fig. 10B). Nuclei in these ooids are micritized and made of bioclastic fragments and peloids. 1.5 m above the beginning of the extinction interval, radial ooids with thicker cortex start to dominate (17% of the total), in a moderately well-sorted grainstone (WM 172, Fig. 10C). These ooids have a diameter between 150 and 900 μm and are still associated with peloids and cortoids. Nuclei are often a peloid, echinoderm, bivalve or gastropod fragment. In most cases, micritization only partially obliterates the original structure, but strong micritization occurs in a minor number of grains (Fig. 10C). In this part of the succession, a few samples include intraclasts with ooids. At 425 m, the sample WM 174 is a bioclastic oolitic grainstone. The majority of ooids are radial or partially micritized, whereas only a minor part is concentric-radial. This grainstone also includes an intraclast with better preserved, radial ooids (Fig. 10D), probably not completely lithified at the time of reworking. In sample WM 178, other intraclasts are present but they appear already lithified during their re-deposition. Point counting performed on six thin-sections (WM 167, WM 168, WM 169, WM 172, WM 173, WM 175) of this interval shows clearly a) the replacement of the peloids by the different types of coated grains which increase from 15% to 64% and b), the gradual replacement of superficially coated grains (the predominant or the only type in samples WM167-169, Fig. 10A) with other coated grains, and a greater diversity of type of coated grains per samples. Micritization has altered most ooids nuclei, but when recognizable they are gastropod or bivalve fragments. In the interval WM 178-WM 183 (425–426 m) oolitic grainstones (with some wackestones and packstones) prevail over micritic/peloidal mudstones. The degree of ooid micritization increases, sometimes completely obliterating the original pattern of the laminae (e.g., sample WM 181, Fig. 10 E-F). Ooids size and cortex thickness decrease progressively upward, with alternations of grainier or peloidal facies (samples WM 186, WM 192, WM 196, WM 198, WM 200-WM 200/20 and WM 201/20; 7 m and upward in Fig. 8, ca. 430–442 m in Fig. S1), Fig. 11 A-D). This trend extends in the following 12 m of the succession in the Sakhra Member. A few samples show the peloidal and grainy thin layers with small ooids (e.g., WM 196, Fig. 11B). In the grainy facies, nuclei are made of peloids or bioclastic fragments. Samples WM 199 and WM 199/20 mark the shift from this dual range in size towards more uniform samples, with peloids often surrounded by a single lamina micritized and partially recrystallized coating. Sample WM 202/20 ends this sequence at the top of a ca. 6 m long packstone/grainstone interval, where the key components are peloids, bioclastic fragments, quartz grains and intraclasts. The next oolitic interval is exposed much higher in the succession, i.e., ca. 50 m above at the lowermost of the following Musandam Formation (Hönig et al., 2017). The basal Musandam Formation samples (WM 204-WM 209) are mostly oolitic grainstones with well-developed and thicker cortices. All these samples exhibit concentric and micritized ooids, except for sample WM 208. In WM 208, ooids are radial and show an excellent preservation with distinct extinction cross at crossed nicols (Fig. 11E). When visible, nuclei are made of bioclastic fragments (e.g.,

Fig. 4. Field picture of the uppermost Sumra Member and of the Sakhra Member. A. Floatstone of the uppermost Sumra Member with frequent calcareous sponges, bryozoan, bivalves and gastropods. B. Coral floatstone with *Retiophyllia* and *Thamnasteria* genera, 1 m below the extinction level (Bed WM 90). C. Last bed before the extinction, still very bioclastic (WM 159). D. Lateral view of the same bed with erosion surface and karstification filled by the overlying orange marls (arrow). E. Top of the flaser bedded interval, just below the first beds with coated grains (WM 95). This is the second erosive surface (arrow). F. Crossbedding in an oolitic grainstone (WM 170). G. Transition from the oolitic grainstone (WM 180) to the peloidal packstone 2.5 m above the extinction level. The circle highlights a dune of oolitic grainstone in the peloidal packstone (WM 181). H. Cross-stratification in the peloidal packstone (WMG 9). (For interpretation of the references to colour in this figure legend, the reader is referred to the web version of this article.)

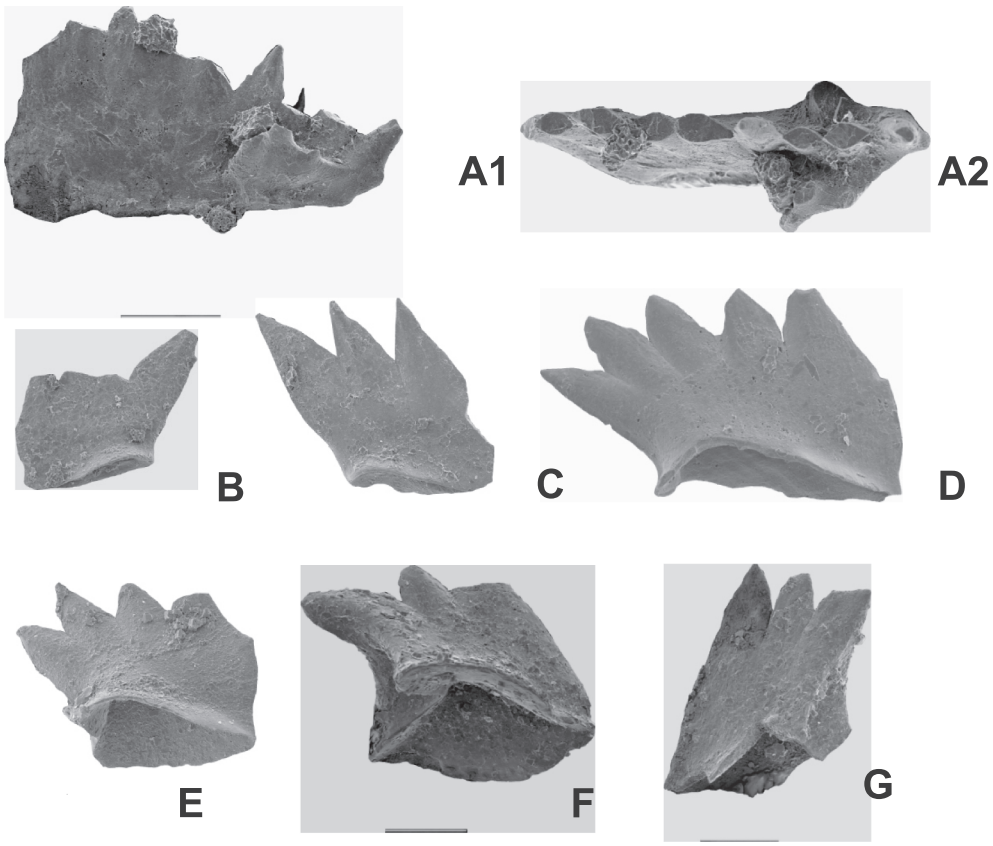

Fig. 5. *Epigondolella bidentata* Mosher, WM 20, lateral view (A1) and upper view (A2). B-D. *Misikella hernsteini* (Mostler), B = WM 32, C = WM 37, D = DQ 288 corresponding to WM 38. E. *Misikella posthernsteini* subsp. A, DQ 292 corresponding to WM 41/42. F-G. *Misikella p. posthernsteini* Kozur and Mock, DQ 337 corresponding to WM 58. B-G. Lateral views. Side bar 100 μm.

bivalves) and peloids.

In summary, radial ooids, and to a lesser extent concentric-radial ooids, are frequent after the extinction interval whereas concentric ooids are present but rare in the Sakhra Member and frequent at the base of the Musandam Formation. Ooids are at first micritized, with an interval of better preservation in the lower part of the Sakhra Member (from WM 172 to WM 175), followed by an increase in micritization more intense than previously. The oolites from the Musandam Formation are preserved without any micritization.

SEM studies show specific microstructures for each group of ooids. The surface of superficially coated grains shows traces of micro-drilling (WM 167; Fig. 12A). The first ooids with multiple-layered cortices (WM 172) show a clear radial pattern with elongated crystals aligning perpendicular to the laminae surface (Fig. 12B). Micritized ooids have an original pattern inside the laminae, replaced by small calcite crystals, randomly disposed, and obliterating the original rims among laminae (WM 181 A; Fig. 12C). In the case of even more micritized ooids with thinner cortices, the cortex is partially recrystallized with small, rounded calcite crystals alternating with bigger and more polygonal ones (WM 197). The interval WM 204 - WM 209 exhibits radial and concentric ooids (see clear radial pattern in WM 208; Fig. 12D). No calcareous nannofossils have been observed in smear slides or under SEM.

4.2.3. Lateral variations

In the laterally adjacent profiles WM2 and WM3, the succession between the uppermost coral-rich floatstone and the first oolitic grainstone is slightly thicker due to interbedding of marls and shale but the number and succession of limestone beds (and their numeration) are similar in all studied sections. An erosion surface is present at profiles WM2 and WM3 at 0 m (Fig. 9), visible as an irregular surface, with small cavities that are filled with the overlying orange marls and small clasts of the surrounding olive-coloured bioclastic limestone. At a regional scale of the Musandam Peninsula, such as in Wadi Naqab and Wadi Sidakh (Senowbari-Daryan and Maurer, 2008; their Fig. 2), slight lateral changes in lithology can be observed below the first oolites of the Sakhra Member, while the basal boundary consistently appears abrupt and erosional. A hiatus is probably present at this level. The base of the succession (0,5–3 m) is more condensed in WM3 with only 1.5 m thickness compared to the 2.5 m at the main section and at WM2. In WM2, some grainy/bioclastic beds are replaced by marly beds (Fig. 9), while in WM3 some beds are missing (Fig. 9). The lateral variability is also reflected in thin sections. The relative proportion of cement, peloids and the total amount of the different types of coated grains change laterally. The amount of bioclasts, micrite, unclassified grains and intraclasts is rather constant (Fig. 9). WM2 175 is an exception with a large number of intraclasts (18%) not seen in any other samples. We observe as well lateral changes through the distribution of the type of coated grains. The first superficially coated grains occur two beds higher in WM3 than in the two other sections (WM3 168 rather than WM and WM2 166 (Fig. 11F)). Radial ooids become a distinct component in the sample WM2 168 (Fig. 11G), in sample 169 in section WM3 and sample 170 in main section. Quartz is seen in intraclasts in samples WM2 168 and WM2 169A, a feature that is absent in other sections. The bed 168 displays strong variations between the amount of cortoids (5 to 13%) and superficially coated grains (1 to 39%) (Fig. 9). The degree of micritization is fairly similar in all sections at this level, with cortoids scattered everywhere. In the succeeding beds, sample WM2 170 is different from sample WM 170, while this grainy horizon is completely absent in the third section. WM 170 includes only superficially coated grains, completely and partially micritized ooids and small radial ooids, whereas WM2 170 A and B display in addition clear concentric and

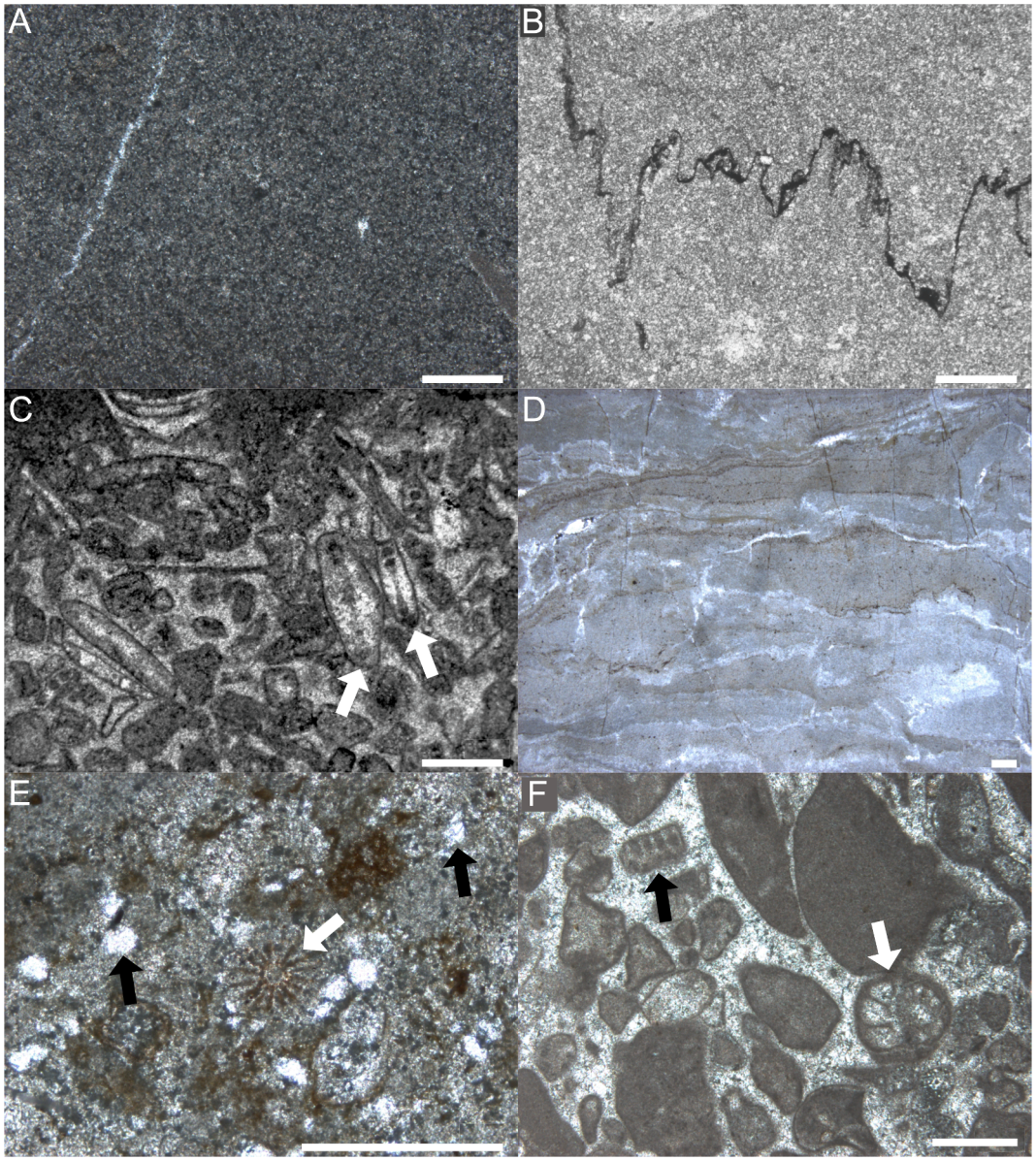

Fig. 6. Thin section observation under petrographic optical microscope of Milaha Formation. A. Dolomitic mudstone in the last dolomitic bed (sample WBDS 71) B. Calcitic mudstone in the first calcitic bed (sample WBDS 72). C. Bioclastic grainstone including the foraminifer *Aulotortus* sp. (sample WBDS 11, white arrows). D. Stromatolite (sample WBDS 29). E. Floatstone with coral fragments (white arrow) and quartz grains (black arrows) (sample WBDS 106). F. Packstone-grainstone with Dasycladacean alga (black arrow) and Duostaminidae foraminifera (white arrow) (sample WBDS 32). Scale bars 500 μm.

radial ooids, with some concentric-radial ooids. In section WM3 quartz grains dispersed in the matrix occur at this level, while in section WM2 quartz is more rare and more concentrated in the intraclasts. Samples 175 are characterized by a great variety of coated grains in all three sections, with the amount of micritization of the grains showing strong variations (Fig. 9). WM2 175 has only 20% of coated grains compared with 56% of WM 175 and 60% of WM3 175. WM 175 contains more concentric ooids, completely and partially micritized ooids and WM3 175 has a sharp dominance of completely micritized ooids respect to all other kinds of coated grains. Concentric-radial ooids are more common in WM2 175 and WM3 175. Quartz grains are scattered in the matrix of WM3 175, while they are included in the numerous intra/extra clasts of WM2 175 and absent in the main WM 175. The interval from samples 178 to 180, displays fairly similar SMF grain size and types of coated grains in all three sections. However, WM2 179 is, in contrast to this interval in the main section, a peloidal grainstone with a higher abundance of quartz and where ooids, with a lower degree of micritization, represent only a minor component of the rock. Samples series WM3 180 (A, B, C, D) are richer in matrix than the main section. In the section WM3 the degree of micritization varies more than in other sections with less micritized samples (e.g., WM3 178A), containing superficially coated grains, radial, concentric and concentric-radial ooids (Fig. 11H) or deeply micritized samples (e.g., WM3 180 D; Fig. 11I).

In summary, the Ghalilah Formation shows a lateral variation that does not affect its general stratigraphy, but which determines a relative condensation or expansion of the ETME interval including the first post-extinction oolite beds. Some differences are noted in the first appearance of specific ooid types during the post-extinction interval (e.g., superficially coated grains, radial and concentric ooids). The quartz content and the degree of micritization vary laterally too.

4.3. $\delta^{18}O_{carb}$ and $\delta^{13}C_{carb}$ analyses of the Wadi Milaha main section

Samples with a strong negative correlation $\delta^{13}C$- $\delta^{18}O_{bulk\text{-}carb}$ and

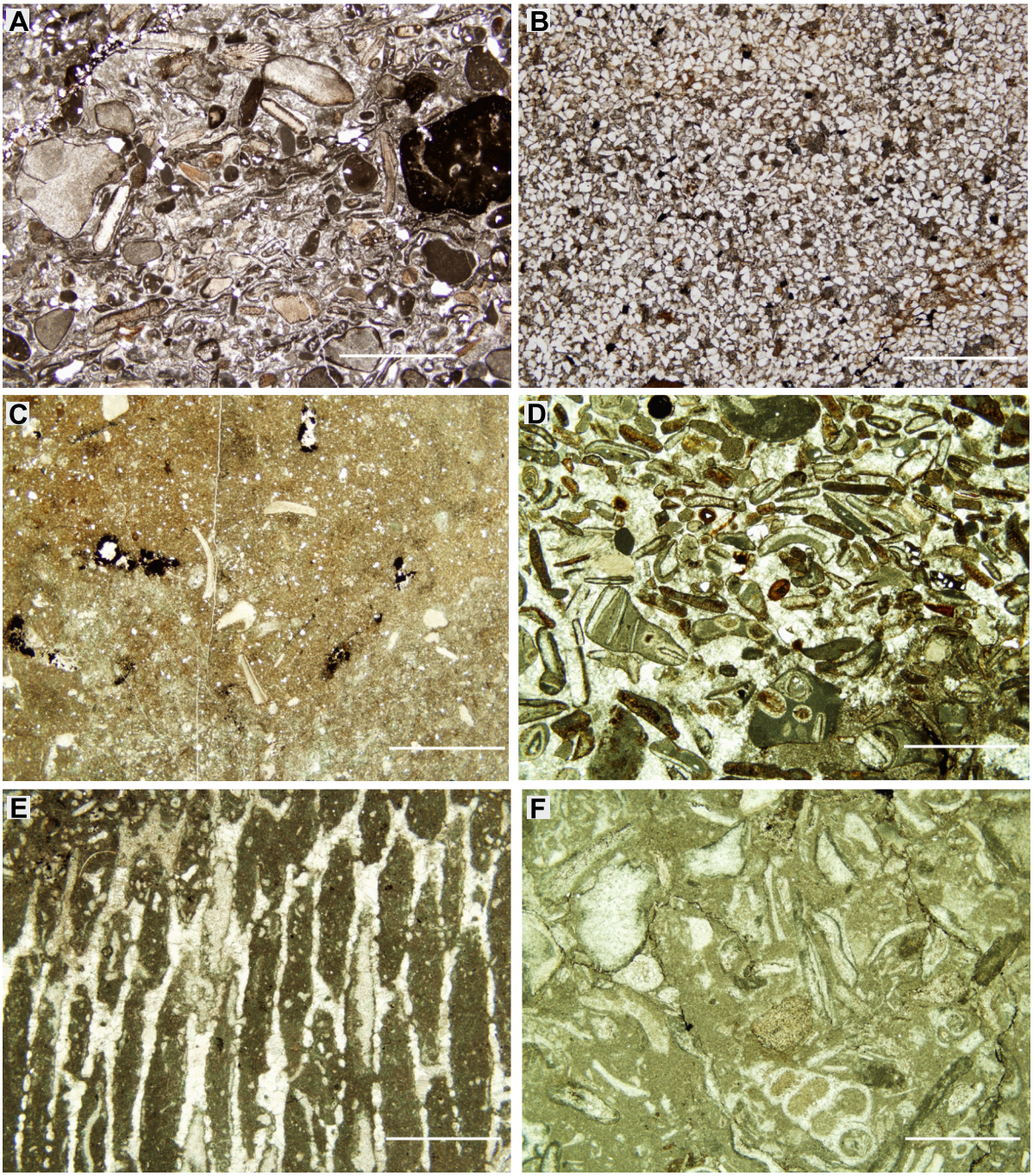

Fig. 7. Thin section observation under petrographic optical microscope of Asfal and Sumra members at Wadi Milaha. A. Packstone with well rounded lithoclasts, echinoderm spines, quartz grains (sample 0411091426), base of Asfal Member. B. Quartz arenite/wacke (sample 0412031140), Asfal Member. C. Mud/wackestone with few crinoids and shells (sample 0412031242), Asfal Member. D. Grainstone with lithoclasts, dasyclads, bivalve shells (sample 0412041540), top Asfal Member, uppermost Norian. E. *Dicerocardium* floatstone (sample 0501201055). First *Dicerocardium* beds, Asfal Member, Rhaetian. F. Rudstone with bivalves, lithoclasts (sample 0501211629), Sumra Member, Rhaetian. Scale bar for all pictures 0.5 mm.

$\delta^{13}C_{bulk\text{-}carb}$ far below the normal marine values (i.e., −3.0 ‰) are shown in Fig. 2 and Table S2 but are considered as outliers and thus not described further. Some points below −3.0 ‰ but with no corresponding very negative $\delta^{18}O_{bulk\text{-}carb}$ values are conserved. The $\delta^{13}C_{bulk\text{-}carb}$ curve for the dolomitic interval (0–138.5 m) starts with a strong decrease of 5.8 ‰ amplitude and is then characterized by negative values from 9 to 72 m, followed by an increase of 3.4‰ until 82 m, and a further slightly increasing trend until the dolomite-calcite boundary within the Milaha Formation (Fig. 2). Two significant positive peaks are seen at 22 m and 37.5 m (both 0.6 ‰). Through the calcite-dolomite boundary (138.5 m), the trend has a 1.5 ‰ decrease and varies with a strong noise around a mean value of 0.1 ‰ until 257 m (lower Asfal Member). A large negative excursion to a minimum of −1.8 ‰ is recorded in the upper Norian (between 259 and 282 m). Above this negative excursion, the $\delta^{13}C_{bulk\text{-}carb}$ curve shows a stable trend around 0.6 ‰, which encompasses the Norian-Rhaetian Boundary, until the end of the Rhaetian. This stable trend shows however, a short negative excursion of 1.4‰ amplitude at the top of the Asfal Member (352–357 m) and two stratigraphically isolated exceptions at 409 m (-2.0 ‰; −4.9 ‰) and 418 m (-1.9 ‰; −8.2 ‰). The first post-extinction bed with coated grains (WM 96, WM 166)

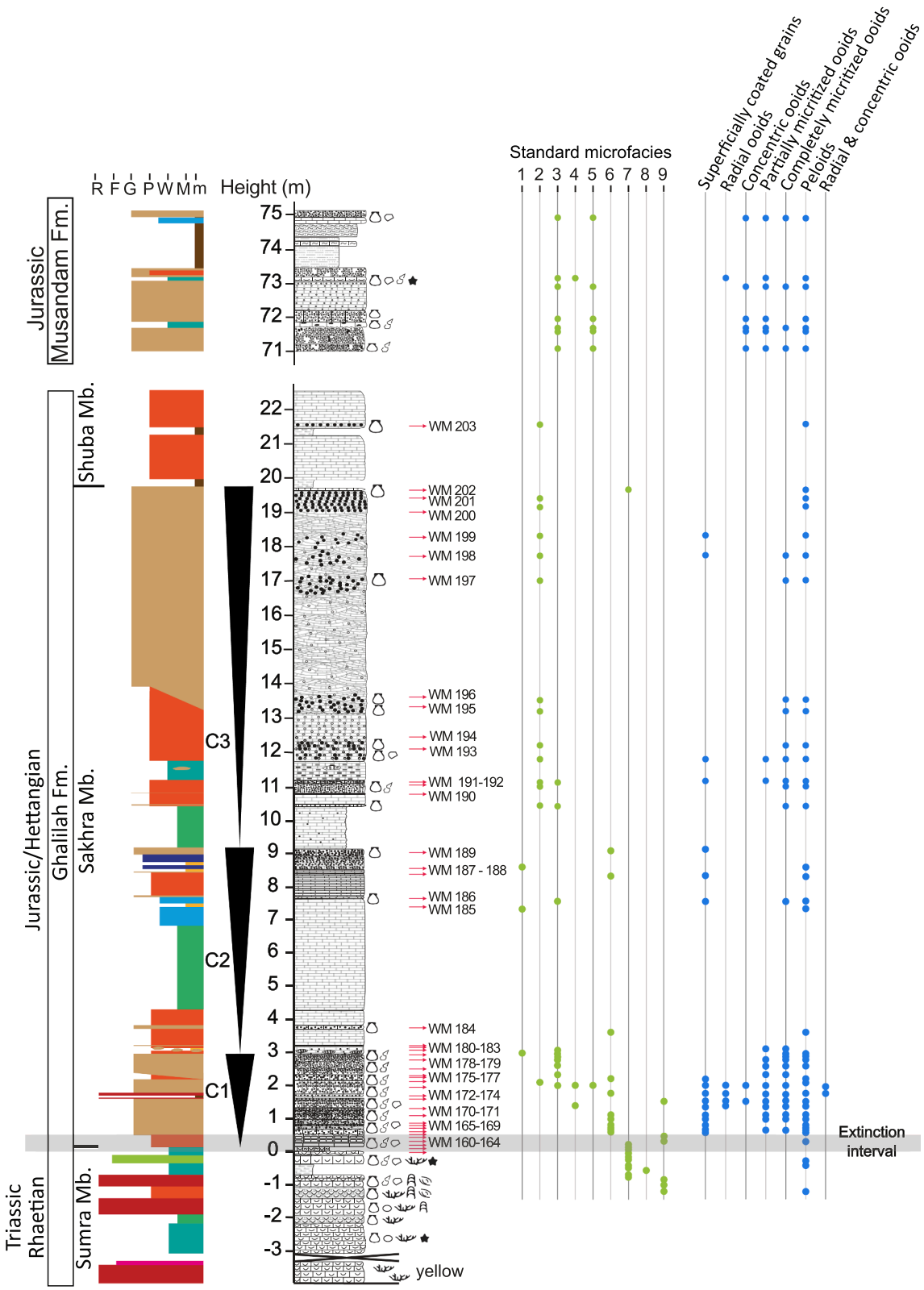

Fig. 8. Detailed stratigraphic log of the Sakhra Member at main Wadi Milaha section with fossil content, type of coated grains, standard microfacies modified from Flügel (2010) and indication of C1, C2 and C3 cycles by Ge et al. (2018, 2019) for comparison. Basal Musandam Formation is also shown. Standard microfacies description: 1. Micritic mudstone with peloids. 2. Non laminated peloidal grainstone or packstone, possibly containing ooids and /or coated grains (modified from Flügel's SMF 16). 3. Micritized ooids grainstone, but also wackestone and packstone (modified from Flügel's SMF 15 M). 4. Radial ooids grainstone (Flügel's SMF 15R). 5. Concentric ooids grainstone, but also wackestone (modified from Flügel's SMF 15C). 6. Grainstone with prevalent skeletal/non skeletal coated grains and/or cortoids. Additional grains are ooids and peloids (modified from Flügel's SMF 11). 7. Bioclastic packstone and wackestone with abraded and worn skeletal grains (Flügel's SMF 10). 8. Wackestone with preserved whole and fragmented fossils (modified from Flügel's SMF 8). 9. Rudstone and grainstone with prevalent densely packed whole fossils and fragments (modified from Flügel's SMF 6).

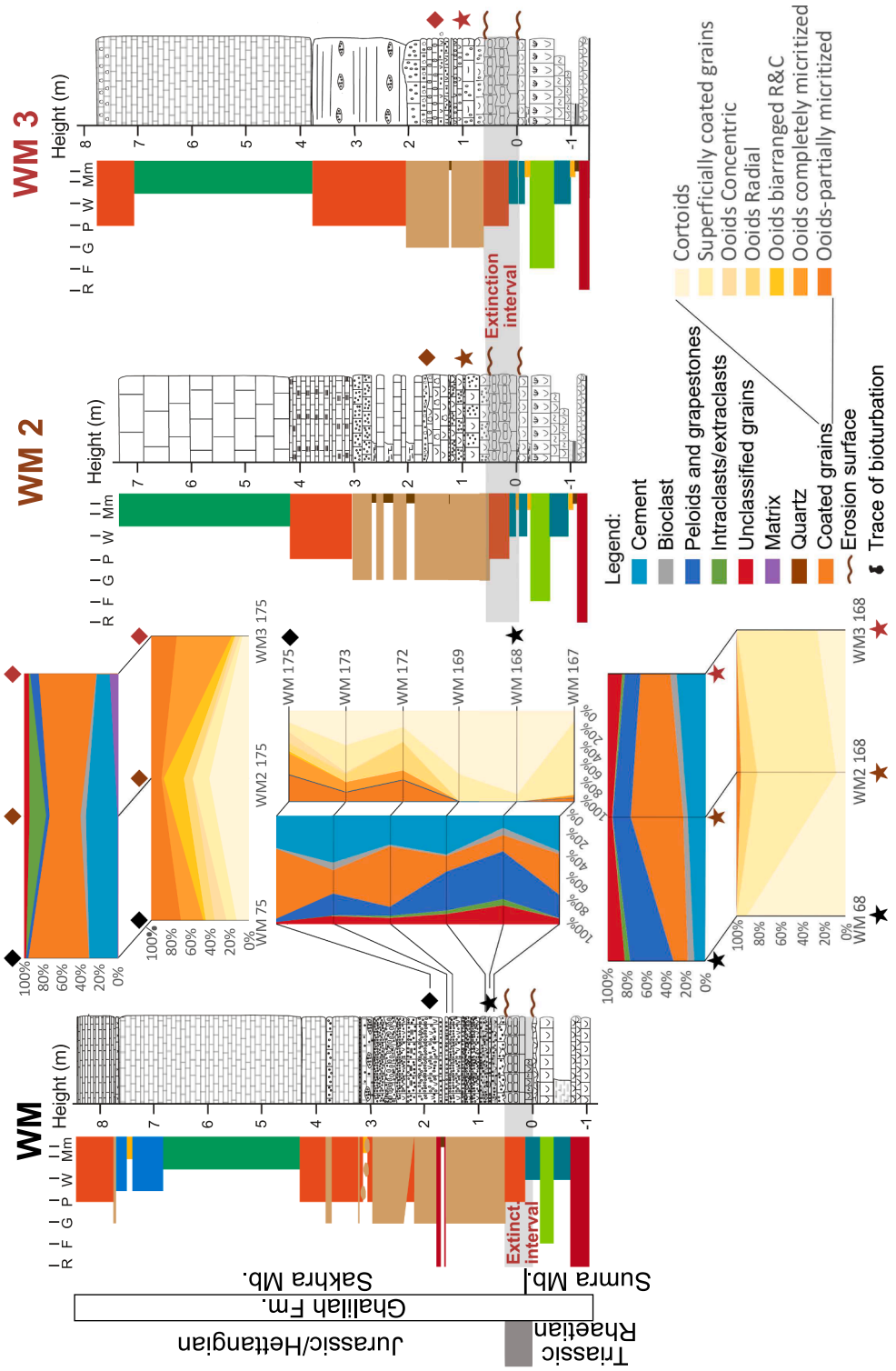

Fig. 9. Stratigraphic logs across the ETME of isochronous sections Wadi Milaha, Wadi Milaha 2 and Wadi Milaha 3. Modal analysis (point counting) of rock components, including different kinds of ooids and coated grains, is displayed for six samples in WM and two samples each in WM2 and WM3.

sees a positive peak to 2.2 ‰ at its base followed by a decrease to 0.6 ‰ higher up and an increase again at 2.7 ‰ in the next bed. The values increase to 4.8 ‰, 8 m above the base of the oolitic grainstone before decreasing through the rest of the Sakhra Member and a major part of the Shuba Member until a minimum of −3.5 ‰ is reached at 484 m. In the uppermost metres of the Shuba Member, a rapid increase up to 1.9 ‰ is shown.

The $\delta^{18}O_{carb}$ trend remains substantially stable within a range of −3 ‰ to 0 ‰ during the dolomite interval in the Milaha Formation with some exceptions at 14 m (-3.9 ‰), 94 m (-3.6 ‰), 103 m (-4.6 ‰), 127 m (-4.1 ‰) and 131 m (-6.7 ‰). The values decrease substantially at the dolomite–calcite boundary; they also show greater variabilities upwards until 340 m but around an average value of −4.8 ‰. From 340 m to the top of the Sumra Member at 423.5 m, the $\delta^{18}O_{carb}$ values are less variable, except for some outliers, around an average value of −4.4 ‰. The $\delta^{18}O_{carb}$ values increase again in variability in the lower Sakhra Member

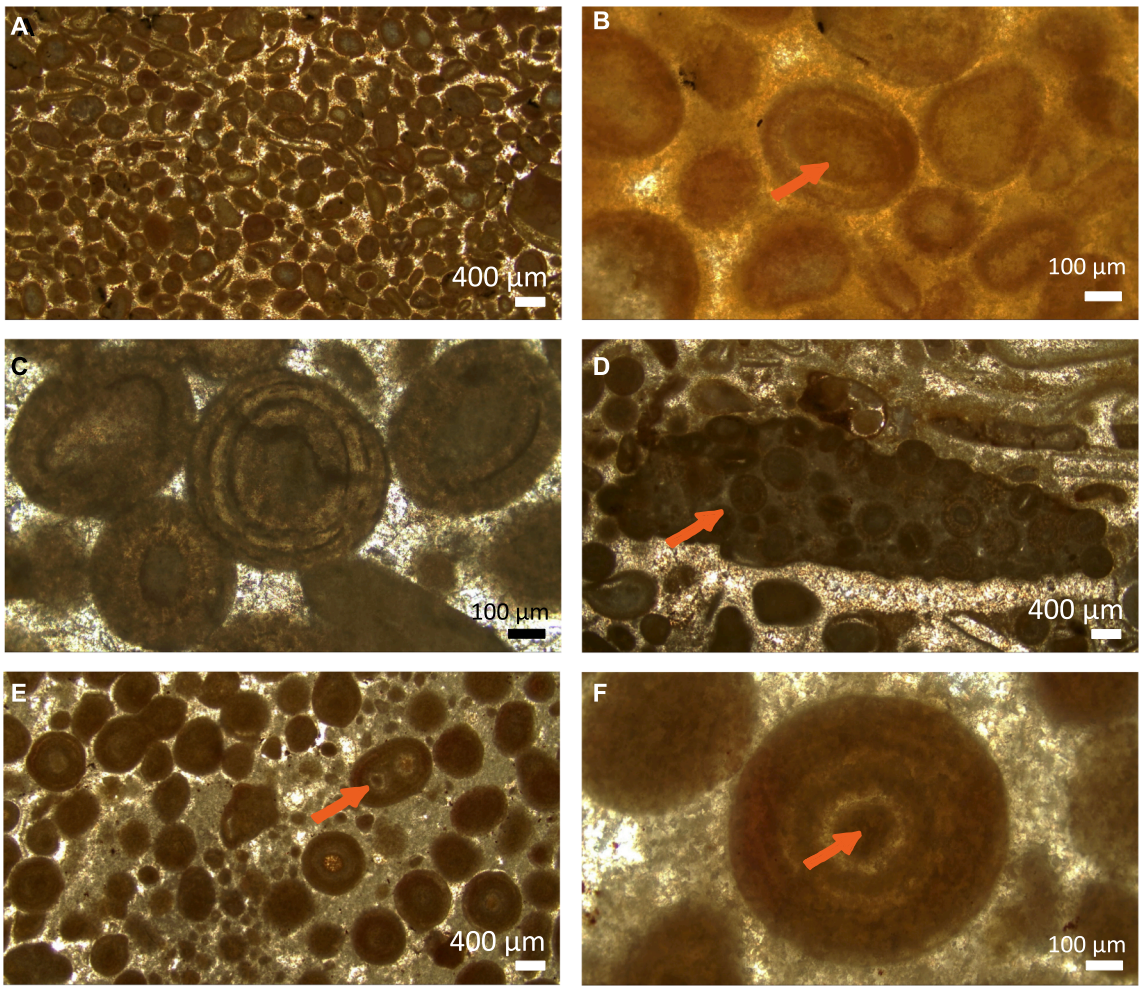

Fig. 10. A. Overview of sample WM 167. Oolitic bioclastic grainstone. B. Sample WM 170. Detail of a partially micritized radial ooid (orange arrow), surrounded by coated grains. Oolitic bioclastic grainstone. C. Sample WM 172. Detail of partially micritized radial ooids. Oolitic/peloidal bioclastic grainstone. D. Sample WM 174. Intraclast (orange arrow) with radial ooids. The whole rock can be classified as a bioclastic oolitic grainstone, while the intraclast itself is more an oolitic packstone. E. Overview of sample WM 181, with a polyooid (orange arrow). Oolitic grainstone. F. Sample WM 181. Micritized ooid with a micritized nucleus (orange arrow), in oolitic grainstone. (For interpretation of the references to colour in this figure legend, the reader is referred to the web version of this article.)

and have a strong increasing trend from −7.9 ‰ till −1.8 ‰ at the top of the Sakhra grainstones. The Shuba Member includes a first negative excursion in its most basal part (448–452 m), followed by values around −1.4 ‰, a second negative excursion in its upper part, with values around −5.5 ‰, and a return to −1.5 ‰.

For the interval around the ETME and the Sakhra Member (422–445 m), $\delta^{13}C_{carb}$ has been measured not only as selected matrix but also by differentiating the cement or the oolitic grains when possible. The matrix, cement and oolite specific curves approximately follow the same trend of the bulk-rock curve with more noise, co-varying with oxygen. In detail, these values increase from 2.3 ‰ in sample WM 166 to 2.7 ‰ in ooids of sample WM 174. The values above are more scattered but show a ca. 3 ‰ negative excursion with a minimum in WM 178. An increase up to 4.5 ‰ is observed in WM 182 followed by scattered values before another decrease at the top of the Sakhra Member.

In the same stratigraphical interval (422–445 m), $\delta^{18}O_{carb}$ values for the selected matrix are more scattered than the corresponding bulk curve before and through the extinction interval (until sample WM 164). The basal interval of the Sakhra Member shows more positive values, while the trend is more similar to the bulk curve going towards the top of the Sakhra Member. The top of the Sakhra Member and the lowermost 2 m of the overlying Shuba Member mark a shift towards more negative values. The isotope curve based on ooids overlaps perfectly with the bulk curve for samples WM 166- WM 172, if one outlier and an extremely negative value (-7.0 ‰ for WM 170) are excluded. The specific curves show more positive values than the bulk rock record until the end of the first oolite horizon (-5.7 ‰ for sample WM 182). Then it appears more adherent again to the bulk curve until the top of the Sakhra Member.

We also take into consideration the cross plots $\delta^{18}O_{carb}$ vs. $\delta^{13}C_{carb}$ for different parts of the succession. In Fig. 13, the dolomite interval (0–138.5 m) shows a resetting of all $\delta^{18}O_{carb}$ around −2 ‰ with larger variability in $\delta^{13}C_{carb}$. The R^2 index for calcitic samples (outliers excluded) in the interval 138.5–495 m is 0.0161 and indicates no clear correlation between the two datasets (Fig. S3). Considering the outliers, the recalculated R^2 is 0.0919 (Fig. 13). In the uppermost meter of the Sumra Member and within the Sakhra Member (samples WM 150-WM 203), the $\delta^{18}O_{carb}$ vs. $\delta^{13}C_{carb}$ cross plot shows no correlation (R^2 = 0.1429, Fig. 14). Even taking into consideration the outliers, a clear meteoric diagenetic pattern with a high water to rock (W/R) ratio is not visible (Lohmann, 1988). Omitting these outliers, linear trend lines reveal a more scattered isotope distribution for ooids and cement, while the matrix data are more aligned to the bulk-rock trend line.

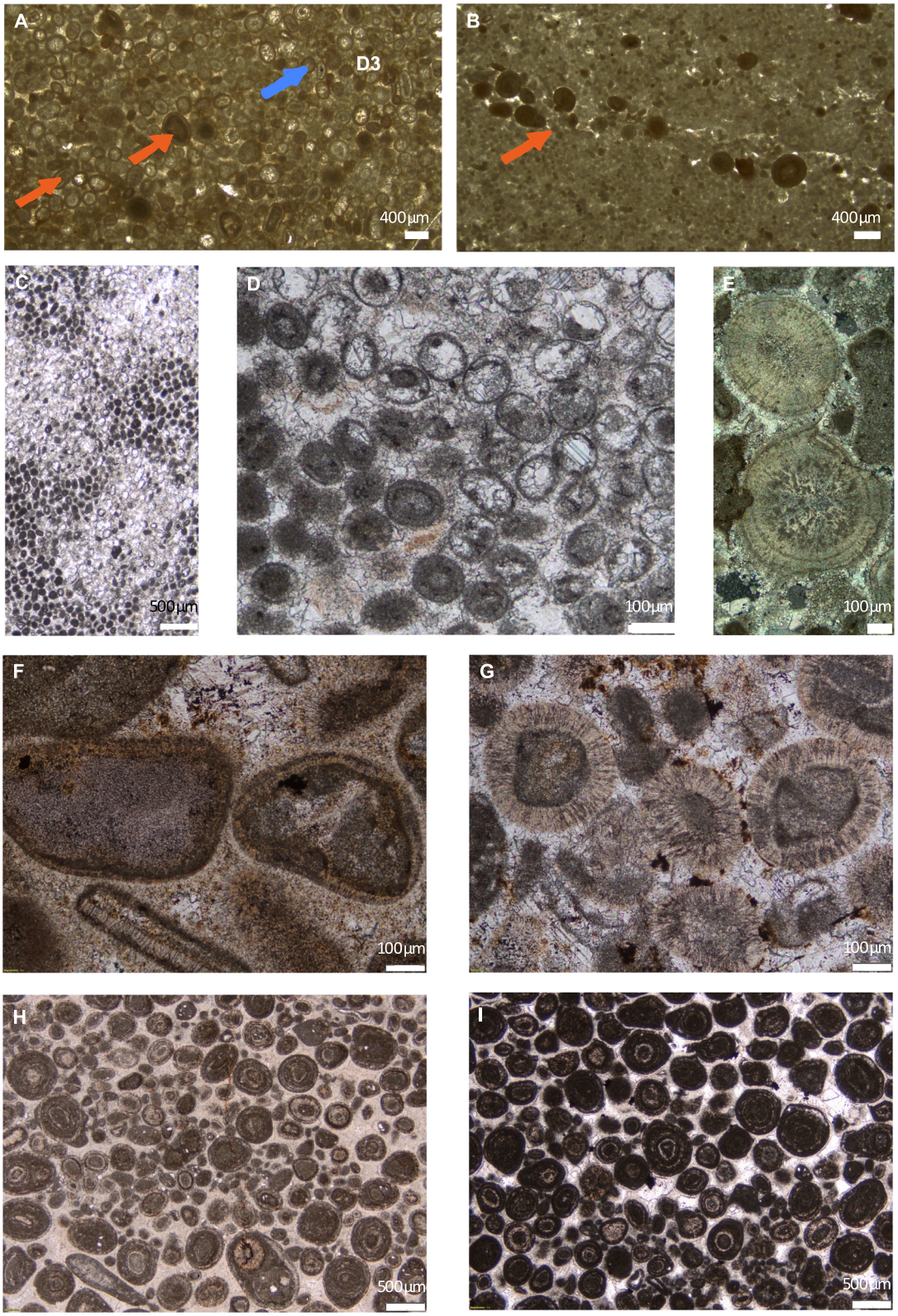

Fig. 11. A. Overview of sample WM 186. Grainstone with ooids (orange arrows) and coated grains (blue arrow). B. Sample WM 196. Ooids arranged on a single line (orange arrow), in a peloidal packstone. C. Sample WM 200/20. Peloidal grainstone. D. Sample WM 201/20. Grainstone with partially recrystallized ooids, E. Sample WM 208. detail of two well preserved radial ooids, showing cross extinction (blue colour) at crossed nicols. Here nuclei cannot be identified. F. Sample WM2 166. Superficially coated grains. G. Sample WM2 168. Radial ooids. H. Sample WM3 178A. Preserved superficially coated grains, radial, concentric and concentric-radial ooids. I. Sample WM3 180 D. Deep micritization displayed in grains. (For interpretation of the references to colour in this figure legend, the reader is referred to the web version of this article.)

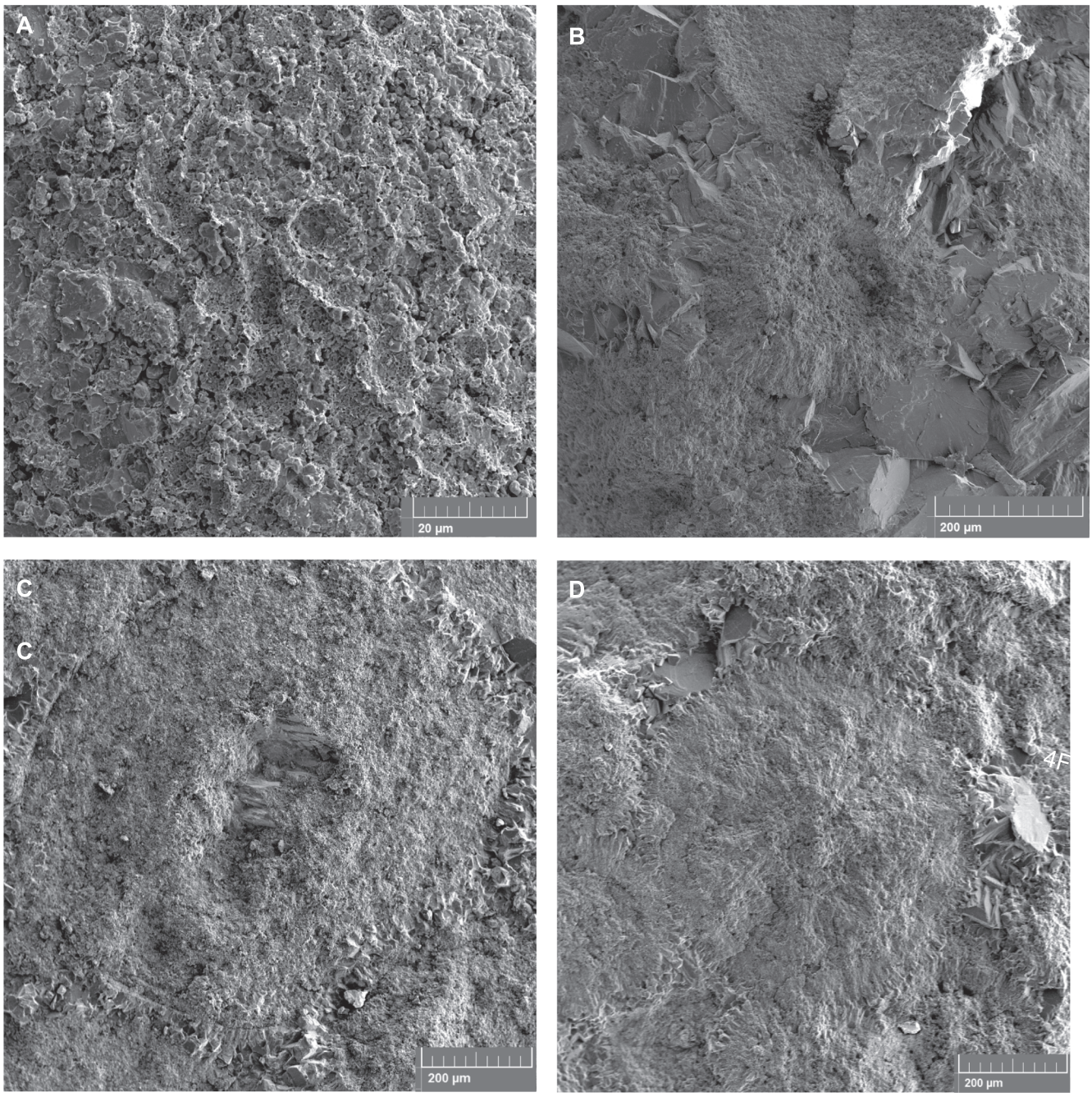

Fig. 12. A. Sample WM 167 at SEM. The surface of a superficially coated grain shows trace of micro drilling. B. Sample WM 172 at SEM. Radial ooid shows cortices with elongated crystals, aligning perpendicular to the laminae surface. C. Sample WM 181 A at SEM. Micritized ooid. The original pattern inside the laminae is replaced by small calcite crystals, randomly disposed, and obliterating the original rims among laminae. D. WM 208 at SEM. Ooid with clear radial pattern.

5. Discussion

5.1. Stratigraphy and biostratigraphy

5.1.1. General

The gradual vertical alternation of facies and their laterally wide continuity reflect the evolution of a low-angle carbonate ramp, marked by a restricted-lagoonal environment at the base of the section (the dolomitic beds). This depositional environment is similar to the limestone beds at the top of the Wadi Milaha Formation and exhibits an oligotypic bio-association. We interpret the intercalation of marlstones in the dolomitic limestones of the Milaha Formation as a deepening upward phase and increase of accommodation space. The following progressive decrease of marlstone sedimentation and the increase in siliciclastic input in the upper Milaha Formation mark a shoaling upward of the succession during a stable sea-level, until the boundary between Milaha and Ghalilah Formation. This boundary is marked by dissolution of megalodont shells in the last carbonate bed and by an intraformational breccia at its top. These probable traces of subaerial exposure lead us to consider it as a sequence boundary. For this Norian part of Milaha Formation, our local sea-level curve seems to reflect the super-regional interpretation of Haq and Al-Qahtani (2005; stable sea-level followed by a sea-level-drop) and is not in contradiction with the global curve of Hesselbo et al. (2007; slowly rising trend).

Alternation of fossil-free sandstones/marlstones/limestones of the lower Asfal Member reflects a restricted subtidal zone (lowstand

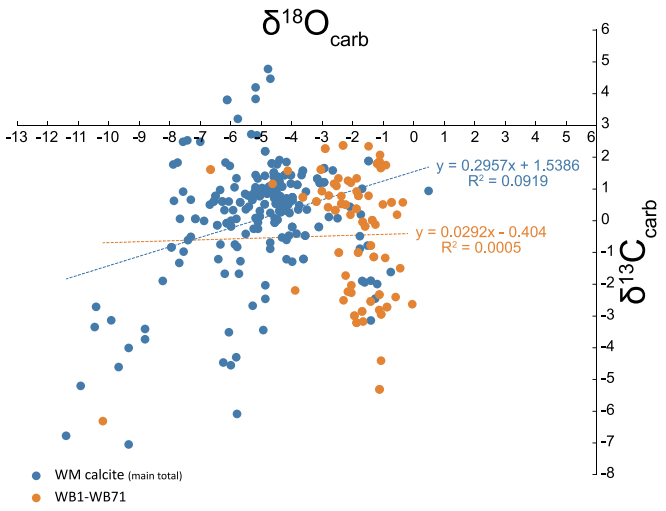

Fig. 13. $\delta^{18}O_{carb}$ vs. $\delta^{13}C_{carb}$ crossplot for dolomitic samples WB 1-WB 71 and for the interval 138.5–495 m (calcite dominated) of the Wadi Milaha section.

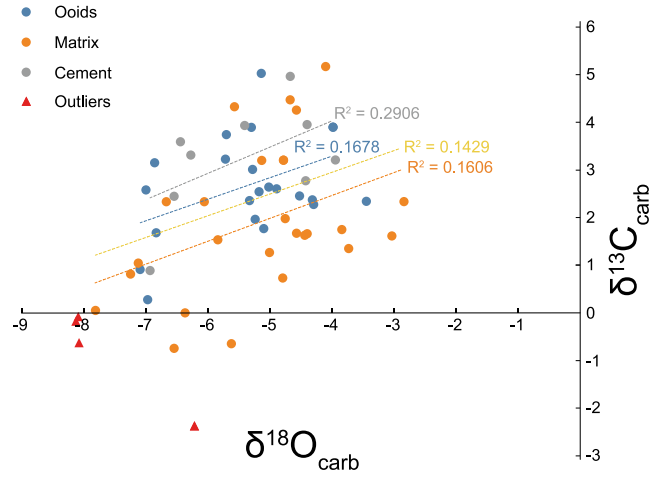

Fig. 14. $\delta^{18}O_{carb}$ vs. $\delta^{13}C_{carb}$ crossplot for the interval 422–445 m (calcite dominated) of the Wadi Milaha section, for sample serie WM 150-WM 203. Four datasets are displayed, distinguishing between different sample components (total, ooids, matrix and cement). Outliers are highlighted separately. Outliers are excluded in Fig. S3. Outliers are here samples with a strong negative correlation $\delta^{13}C$- $\delta^{18}O_{bulk\text{-}carb}$ and $\delta^{13}C_{bulk\text{-}carb}$ far below the normal marine values (i.e., below −3.0 ‰); some points below −3.0 ‰ but with no corresponding very negative $\delta^{18}O_{bulk\text{-}carb}$ values are conserved.

system). From 270 m onward, the transition to a more open subtidal zone is highlighted by the appearance of open marine (brachiopods, bivalves) and even pelagic organisms (conodonts, ammonoids) and reflects a transgressive system. With onset of the *Dicerocardium* beds at 316 m in the upper half of the Asfal Member starts a regressive trend interpretable as highstand system. The Asfal-Sumra Boundary, above the last *Dicerocardium* bed, records the change from subtidal carbonate-rich lagoon to more proximal shallow-water siliciclastics and is probably another sequence boundary. The drop of the base level under the present-day mean sea level associated by Haq (2018) to the NRB, could eventually thus correlate rather to the Asfal-Sumra boundary in Wadi Milaha despite its attenuated amplitude. The first beds of the Sumra Member are characterized by rather shallow water bivalves (*Placunopsis* lumachelles). Above, alternations of marlstones and limestones without quartz input and multiple occurrences of *Retiophyllia* and thamnasteriid coral rudstones/floatstones at the very top suggest the gradual shift from a restricted subtidal zone to more open subtidal zone again (Senowbari-Daryan and Maurer, 2008). This could correspond either to a gradual but constant sea-level rise (Hesselbo et al., 2007) or a more pronounced rise followed by a stable sea-level at the top of the member (Hallam and Wignall, 1999) but not to a stable phase as hypothesized by Haq and Al-Qahtani (2005). The top of the Sumra Member is developed with two erosional surfaces, extensively described in the Triassic-Jurassic boundary subchapter of this discussion. It marks probably a pronounced type I sequence boundary associated with the global regression linked to the CAMP events (Lindström et al., 2021), in clear contradiction with the interpretation of Hönig et al. (2017) to be a maximum flooding surface (at the base of their "Rhaetian 1").

The Sakhra Member lithofacies could be interpreted as an open platform environment and high energy shoals where grainstone and packstone facies are prevalent. However, the specific geochemical characteristics of oceanic waters in the post-extinction world with high concentrations of dissolved calcium carbonate, low redox conditions and high nutrients could have driven these massive, meter-scale oolitic facies to develop not only in their classical sedimentological settings (e.g., in terms of wave energy or open ramp). Indeed, their position just above a subaerial erosive surface and below peloidal packstone typical of lagoonal conditions speaks rather for changes in deposition conditions on the upper ramp rather than a very rapid transgression-regression cycle. The Shuba Member represents poorly fossiliferous facies that include marlstones, dolomitic mudstones and siltstones, at some levels with desiccation cracks. The depositional environment is interpreted as restricted and most probably lagoonal. The sea level tends to gradually fall, as proposed by Hesselbo et al. (2007) and opposed to the assumptions of Hallam and Wignall (1999).

In terms of sequence stratigraphy, a general transgressive trend is seen, with deposition of Jurassic facies at the highstand (aggradation phase). The low angle of the ramp prevents the transgressive regime to establish deeper marine conditions. More in detail, it is possible to assign the mid to upper Norian Wadi Milaha Formation to a highstand systems tract (HST), which culminates in a sequence boundary with trace of erosion (intraformational conglomerate at 252 m), the latter probably representing the falling stage systems tract, FSST. The basal Asfal Member is interpreted as the succeeding lowstand systems tract until the number of sandstones beds starts to decrease and is replaced by an alternation of marlstones and limestone with more marine open organisms (above 270 m), which marks the start of the transgressive systems track. The *Dicerocardium* beds interval (upper Asfal Member) represents probably an highstand with a marked regression at the top. The following Sumra Member is interpreted as the following transgressive systems tract (TST). The regression linked to the end-Triassic Mass Extinction is here clearly seen. The presence of desiccation tracks marking subaerial exposure in the Shuba Member reflects a regression which could be interpreted either as low stand or highstand. In the first case, the first meters of the Sakhra Member with the well-developed oolites will be interpreted as the TST, followed by a highstand for the rest of the Sakhra Member. The sequence boundary is then set at the top of the last massive grainstone bed at 442.5 m. In the second case, the full Sakhra Member is interpreted as TST and the Shuba Member as highstand. Further studies should help to decide between the two solutions.

5.1.2. *The Norian-Rhaetian boundary in Wadi Milaha*

The NRB in the Wadi Milaha section occurs in the upper part of a mixed carbonate-siliciclastic succession. The boundary level is delimited by the occurrence of the Norian assemblage of the conodont *Epigondolella bidentata* and the ammonoid *Neotibetites* sp. at 274 m and the presence of the ammonoid *Neotibetites weteringi* at 299 m. The Dawhat Qabal section in the Oman part of the Musandam (N 26° 01′ 57.0″ E 56° 22′ 39,5″, Jabal Sall Ala section in Hönig et al., 2017; Fig. 1A) yielded more conodonts in the strata bracketing the boundary. The Dawhat Qabal section is easily correlated to the Wadi Milaha through marker beds like the three massive limestone beds at 312–314 m: 316–318 m

and the first *Dicerocardium* bed at 320–322 m. The bed at 299 m recording *Neotibetites weteringi* contains in Dawhat Qabal also *Misikella hernsteini*. The Norian assemblage *Parvigondolella andrusovi-Misikella hernsteini* has been found 2,5 m below the marker bed at 312–314 m (WM 37). The Rhaetian assemblage with frequent *Misikella hernsteini* and rare *Misikella posthernsteini A* sensu lato has been found in Dawhat Qabal below the first marker bed at 312 m (equivalent WM 38) and 320 m (equivalent WM 41/42) bracketing the Norian-Rhaetian Boundary between 309 and 312 m, 8 m below the first *Dicerocardium* beds.

The Rhaetian GSSP is still not defined and currently, two proposed candidates in Austria (Steinbergkogel) and Italy (Pignola Abriola) are discussed. Both options depend on two different morphotypes for *Mi. posthernsteini*—A sensu lato (s.l.; Austria candidate) and B sensu stricto (s.str.; Italian candidate). Based on magneto-stratigraphic correlation with the continental Newark Basin, dated with a highly debated *cyclo*-stratigraphy (e.g., Olsen et al., 2010; Maron et al., 2015; Tanner and Lucas, 2015; Weems et al., 2016; Kent et al., 2017), Maron et al. (2015) and Rigo et al. (2016) proposed a paleontologically and sedimentologically unlikely 4 million years interval between these two morphotypes in Italy. Whereas Galbrun et al. (2020), based on cyclostratigraphy on Steinbergkogel proposed a duration inferior to a long eccentricity cycle (400′000 years) for the interval between the two morphotypes. The Norian-Rhaetian boundary is here defined with *Mi. posthernsteini* A. in comparison with Steinbergkogel. Unfortunately, no conodonts have been found between the first and third *Dicerocardium* beds either in Wadi Milaha or in Dawhat Qabal. However, the top of the third *Dicerocardium* bed at Dawhat Qabal (equivalent to WM57 at 355 m in Wadi Milaha) has delivered a rich population (100 specim.) of *Mi. posthernsteini* B. As a consequence, the Norian-Rhaetian boundary *sensu* the Italian candidate is somewhere floating within an interval of 35 m between 316 and 355 m (WM 41/42 and WM 57). It is to be noted that two levels of *Heterastridium* (Marcoux et al., 1993; Flügel, 2010) have been found at 337 and 349 m respectively. *Heterastridium* was thought to mark the upper Norian but is here lowermost Rhaetian.

5.1.3. The Triassic-Jurassic boundary in Wadi Milaha

The exact location of the Triassic-Jurassic Boundary (TJB) along the Wadi Milaha section is still debated. Maurer et al. (2008, 2009) proposed the TJB at the top of the coralline framestones (Sumra Member). These strata are overlain by poorly fossiliferous beds, typical of post-extinction deposition. Late Triassic Retiophyllia corals with a rich lagoonal and patch reef fauna are found in the upper Sumra Member of our Main Wadi Milaha section, whereas Jurassic bivalves (*Liostrea*- and *Modiolus*-like) are found in the lower part of the Sakhra Member. A single occurrence of the foraminifer *Orbitopsella*, assigned by Glennie et al. (1974) as of early Jurassic age (Maurer et al., 2008, 2015; Al-Suwaidi et al., 2016; Ge et al., 2018) supports this hypothesis. The same definition was followed by Al-Suwaidi et al. (2016); Ge et al. (2018, 2019) and Ge (2021). However, these latter authors argue that the TJB corresponded to a minor negative excursion in the $\delta^{13}C_{carb}$ record at the base of Sakhra Member, which we were not able to reproduce here, all the small negative inflections being probably a result of diagenetic influences.

Instead, de Matos (1997) and later Hönig et al. (2017) set the TJB in the uppermost Shuba Member. They did not confirm the finding of *Orbitopsella* in their samples from the Shuba Member and instead documented the presence of the Triassic long-lasting shark teeth (*Acrodus* cf. *lateralis*) and bivalves (*Pseudoplacunopsis* sp., *Plicatula radiata*, *Bakevillia* sp.) in this member, as opposed to early Jurassic crinoids (*Balanocrinus subteroides)* in the basal part of the overlying Musandam Limestone. They also associated a record of the green algae *Palaeodasycladus* sp. to the Shuba Member. Some of these biostratigraphic markers were questioned by Ge et al. (2018), as none of the bivalves presented can be assigned only to a Triassic age and the type locality of *Palaeodasycladus* sp. genus is dated to early Jurassic (Ge et al., 2018; Barattolo et al., 1994). In addition, Hönig et al. (2017) presented an $^{87}Sr/^{86}Sr$ age determination of the supposed TJB in the neighbouring Wadi Naqab section, which did not prove resolute. In this study, we follow the approach of Maurer et al. (2008). We motivate our choice by the absence of a solid palaeontological record to assign a Triassic age to both Sumra and Sakhra members. Besides, we confirmed a substantial change in the faunal assemblages from the Sakhra to Sumra members, including a shift from strata yielding a rich Late Triassic fauna to strata with a post-extinction depositional character, including scarce bioclasts, rare small bivalves and a predominance of abiotically or microbially mediated ooids. The bivalve pavement in the lower beds, even if not determinable, resembles the characteristic post-extinction bivalve pavement of the Blue Lias Formation in England. In addition to the observations of Ge et al. (2018, 2019) and Al-Suwaidi et al. (2016), we also document two erosion surfaces in the uppermost Sumra Member in our studied sections. The first surface is smooth in the main section, but at WM 2 and WM 3, small cavities in the surface are filled with both the overlying orange marls and small clasts of the same olive bioclastic limestone, marking a short transport of clasts. At Wadi Milaha, there is no sign that this hiatus could be due to subaerial erosion as there are no such cavities or any signs of soil-forming processes. The second post-extinction grainstone is also marked with irregular surfaces and orange filling. The irregularity of the surface testifies to partial dissolution of the limestone and could be also due to submarine erosion. However, at a regional scale of the Musandam Peninsula, these levels appear always sharp and erosional (Senowbari-Daryan and Maurer, 2008) and sometimes deep karstification has been observed as in Wadi Naqab (Fig. 1A). This subaerial exposure is to be correlated to the important regression documented elsewhere at the ETME (Lindström et al., 2021). In the absence of conclusive argument, the two erosive surfaces during the ETME interval at Wadi Milaha can be interpreted either as submarine as consequence of an acidifcation event or subaerial and consequence of the regression.

The in situ breccia is a very local phenomenon, which, laterally, reaches downwards to different horizons but whose top is always, when present, the second erosive horizon. We interpret it as a seismic event. It is interesting that its position just after the mass-extinction level, is similar to the numerous seismites recorded in the epicontinental sections of NW Europe at the same time and associated to the CAMP activity (Lindström et al., 2015). However, the unknown duration of the hiatus associated with the first surface erosion and the lack of good biostratigraphic control during this interval do not allow to correlate it to this seismic activity with certitude.

The transgressive phase postdating the extinction interval in our section is coherent with similar transgressive trends detected in other Hettangian sections around the world (Pálfy et al., 2021). For the Dachstein platform in the Northern Calcareous Alps, Pálfy et al. (2021) associated this transgression to the drowning of margin reefs and the subsequent transition from rimmed platforms to carbonate ramps. The demise of reef builders was a direct cause of ocean acidification events during the ETME. The so-called “unreefing” model was thus proposed to explain this phenomenon for the northern latitude reefal systems only. It was supposed not to have occurred in southern latitude platforms, including the Arabian platform (Ge et al., 2018; Pálfy et al., 2021). Sections more proximal to the Arabian Shield have been interpreted to be associated with a longer-lasting hiatus (Carnian to Sinemurian?) probably due to the Cimmerian orogenesis (Szabo and Keradpir, 1978, Sharland et al., 2001; Obermaier et al., 2012, Stewart, 2016, Issautier et al., 2019); unfortunately, the exact range of the hiatus is often difficult to determine due to the lack of age-diagnostic fossils. Due to this large hiatus in the surrounding areas, it is not clear where and if a reef was in place off the lagoonal to upper-ramp depositional environment of the Wadi Milaha succession and how it was affected by the end-Triassic crisis. Still, the substantial changes in facies across the TJB interval (from coral-rich rudstones/floatstones to less fossiliferous packstone/grainstones, full of ooids) suggest that a stop in productivity could have caused this apparent transgressive trend, or at least enhanced the

apparent transgression at the Sakhra-Shuba members transition. The deposition of extensive post-ETME ooids along the Wadi Milaha section can moreover have been favoured by high bicarbonate concentration due to the underlying acidification and the weakness of carbonate biomineralization in the low diversity ecosystems typical of these post-extinction oceans. These observations in Wadi Milaha would eventually extend the "unreefing" model approach to more southern latitude platforms.

5.2. $\delta^{13}C_{carb}$ and $\delta^{18}O_{carb}$ isotopes

Both the $\delta^{13}C_{carb}$ and $\delta^{18}O_{carb}$ trends presented in this paper extend from the middle Norian to the Hettangian. This time interval was subject to several studies of isotopic trends worldwide (see review in Rigo et al., 2020; Kovács, 2021). However, our record is the longest continuous $\delta^{13}C_{carb}$ record in one single section with biostratigraphic control until now. Although our curves show some outliers, the general trends are consistent with sections elsewhere presented in the literature. The outliers show very negative values in both $\delta^{13}C_{carb}$ and $\delta^{18}O_{carb}$. Considering the shallow depositional setting, the overall low burial diagenesis of the area, and the very negative values obtained in both carbon and oxygen isotopes, these outliers most likely represent short-term influences of meteoritic waters. The fact that these single point negative shifts are often associated with a limestone whose top is encrusted and overlain by a prominent shale/sandstone interval reinforces this interpretation. Disregarding these outliers, cross plots $\delta^{18}O_{carb}$ vs. $\delta^{13}C_{carb}$ show no correlation and the preserved signal probably reflects the original marine composition at least for the carbon isotope record.

A 1.5 ‰ long-term decreasing trend through the entire Norian has been recorded from Italy, Greece (Muttoni et al., 2014), Austria and Oman (Kovács, 2021) with two intervals of accelerated decrease, at the base of the Lacian (earlier than in our record) and in the Alaunian (Muttoni et al. (2004, 2014); Kovács, 2021). However, the lower part of our curve (0–75 m) represents a large negative peak rather than this long-term decreasing trend. Muttoni et al. (2004, 2014) recorded in the Pizzo Mondello section (Italy) an additional negative excursion in the Alaunian 2, which could correspond to our excursion. However, this excursion was not recorded in the Alaunian of Silická Brezová (Slovakia; Korte et al., 2005) or in Leislingkogel (Austria; Kovács, 2021). In Pizzo Mondello, this negative excursion shows a strong correlation between the $\delta^{13}C_{carb}$ and $\delta^{18}O_{carb}$ values in opposition to the rest of the section and could represent a diagenetic feature (Muttoni et al., 2014). In Wadi Milaha, this negative excursion occurs in the shallower part of the section with the most restricted facies, prone to early dolomitization and could be influenced by meteoric water or record local development. On the other hand, as the record in Silická Brezová in the Alaunian 2 is scarce (Korte et al., 2005) and this interval is particularly condensed in Leislingkogel (Kovács, 2021), this negative shift could have been missed in both sections. Further studies will thus be necessary to conclude about the presence or absence of an isotopic perturbation in the middle Norian. Above, between ca. 139 to 169 m, there is a decrease from 1.2 ‰ in average to 0.1‰ in average. This decrease starts just above the boundary between dolomite and calcite at 138.5 m and could be due to the passage from one lithofacies unit to the other. It could represent alternatively the accelerated decrease in $\delta^{13}C_{carb}$ in the Alaunian (Muttoni et al., 2014; Kovács, 2021). In the latter case, the lower negative peak in the dolomitic part of our section could not be correlated to the negative peak in Pizzo Mondello, as this one occurs above the Alaunian $\delta^{13}C_{carb}$ accelerated decrease. Upward, the trend is very stable across the NRB until the ETME. We were unable to reproduce in this $\delta^{13}C_{carb}$ record the "chaotic carbon interval" seen by Zaffani et al. (2017, 2018) in their $\delta^{13}C_{org}$ record. Rigo et al. (2020) claim a negative peak in $\delta^{13}C_{org}$ at the NRB in different sections. However, Kovács (2021) suggests that 1) these negative peaks are not well correlatable and may not be global and 2) the $\delta^{13}C_{carb}$ in many Tethyan sections does not present any negative excursion. There is potentially a negative shift of around −2.0 ‰ between 268 and 280 m thus 30 m below the NRB. This interval is rich in siliciclastic strata and the $\delta^{13}C_{carb}$ minimum is reached in a limestone with trace of aerial erosion (at 273 m) and is probably due to diagenesis. Moreover, there is no such excursion recorded around the Alaunian-Sevatian boundary in any other section (Richoz et al., 2008; Richoz and Krystyn, 2015). Another negative peak from 0.5‰ to −0.8‰ occurs at 354 m, 40 m above the NRB.

In our section, no negative shift corresponding to the late Triassic initial CIE is recorded through the extinction interval (422–423.5 m), in contrast to e.g., the GSSP section Kuhjoch (Ruhl et al., 2009; Hillebrandt et al., 2013). The interval between 402 and 418 m is noisy and shows several excursions which could be of diagenetic origin. Three metres below the extinction level, the curve shows a 1 ‰ increase but then stays constant. The absence of this negative shift can be due to a lack of deposition, marked by the erosion surface at 0 m in our studied sections. Above, a positive shift starts with the ooids deposition. A similar positive shift is seen at the base of the extinction interval between the "marshi" (initial) and "spelae" (main) CIE in several European sections (Lindström et al., 2017), including the Kuhjoch section (Ruhl et al., 2009; Hillebrandt et al., 2013). Another positive peak is seen at the base of the Psiloceras *tilmanni* Zone above the "spelae" CIE (e.g., Lindström et al., 2017). This early Hettangian positive trend is topped in many sections by a shift towards more negative values around the *P. Planorbis* Zone, followed by a more stable trend (Hesselbo et al., 2002; Bartolini et al., 2012; Lindström et al., 2017; Ruhl et al., 2020, Pálfy et al., 2021). Pálfy et al. (2021) correlated this second positive trend with the one of same amplitude in Wadi Milaha section presented by Al-Suwaidi et al. (2016) and Ge et al. (2018). On the other hand, Bartolini et al. (2012) argued that the $\delta^{13}C_{org}$ record of some sections (New York Canyon, Kennecott Point and to a lesser extent Lyme Regis) registered a wide positive shift (~5 ‰ for the first two sections, ~4 ‰ for the third one) in the late Hettangian *Angulata* ammonite Zone; this major excursion was previously attributed to early Hettangian by Williford et al. (2007). If this were the case for our Wadi Milaha section, the erosive surface in the upper Sumra Member would represent a bigger gap in our stratigraphy. The temporal extension of our gap thus remains unclear, due to limited biostratigraphic constraints: it could represent just the *marshi* CIE, the whole post extinction interval of Kuhjoch, or even the whole early Hettangian.

5.3. End-Triassic mass extinction ooids

The coated grains deposited in the early aftermath of the ETME in the main Wadi Milaha section show a specific stratigraphic trend characterized by both a significant diversification in morphology of the coated grains and change in their size. A certain variability was already detected by Ge et al. (2018, 2019). These studies presented a different classification and distribution of coated grains. Ge et al. (2018, 2019) subdivided the Sakhra Member into three coarsening-upward cycles, named C1, C2 and C3. These three cycles are developed in the Sakhra Member of our main section as well. In contrast to the study of Ge et al. (2019), we found that only C1 shows a clear coarsening upward pattern with significantly bigger ooids at the top. However, C1 does not show a prevalence of concentric-radial ooids in any of our three sections; such ooids are only one of the types of coated grains that constitute the C1 cycle. Superficially coated grains are the main constituents of the first meter after the ETME interval, with an upward shift towards an assemblage richer in radial ooids. During the deposition of superficially coated grains close to the ETME interval, dissolved bicarbonate concentration, redox conditions, nutrients supply and water energy regime can potentially prevent or favour the growth of cortices around the nucleus. The ocean could have been supersaturated in respect to $CaCO_3$ during the aftermath of the mass extinction due to 1) an increased continental weathering caused by deteriorated vegetation protection and acid rains (Ahlberg et al., 2003; van de Schootbrugge et al., 2020; Shen et al., 2022), 2) the large absence of organisms able to precipitate

organic-related carbonate (Hillebrandt et al., 2013; Pálfy et al., 2021), 3) rebound after large carbonate dissolution associated with an acidification event (Greene et al., 2012a; Bachan et al. (2012, 2014); Jost et al., 2017). However, it has been suggested that supersaturation alone is insufficient to precipitate carbonate (Diaz and Eberli, 2019). If we consider bacteria as an important catalyst in forming ooids, they need a certain nutrient flux to promote the precipitation of carbonate layers around a nucleus. Batchelor et al. (2018) hypothesized that ooids grow in a biofilm whose outer layer receives diffusing nutrients at a constant rate per unit of time. We suppose that initial layers around nuclei can accrete in a post-extinction environment supersaturated with respect to $CaCO_3$ when the nutrients supply is enough to trigger microbial activity. However, the minimum amount of required nutrients can be lower than expected if water is extremely supersaturated. Microbial consortia include among other photosynthetic and sulphate-reducing bacteria, with the latter increasing the Saturation Index of the $CaCO_3$ in marine and hypersaline water, favouring its precipitation (Dupraz et al., 2009). The oxygenation rate (i.e., either oxic or dysoxic conditions) in water can favour one of these two co-living assemblages and modify the way how they hack into the process of carbonate precipitation. The complexity of mechanisms regulating microbial-mediated precipitation of carbonates is even enhanced if coupled with water energy: indeed, when the precipitation occurs in a low energy environment, the degassing of CO_2 and subsequent precipitation of $CaCO_3$ is prevented. We, therefore, propose that the precipitation of initial post-extinction superficially coated grains could have been triggered either in an alternatively oxic or dysoxic, low-energy environment with sufficient nutrient supply or in the presence of supersaturated water. Subsequently deposited thick-laminated ooids could have formed thanks to a combination of factors, e.g., higher nutrients supply, higher water energy or an enhanced carbonate saturation. The occurrence of less and more coated grained assemblages after the extinction event can thus be seen as a process that combines global seawater chemistry parameters and local sedimentological driving factors. The first appearance of concentric-radial ooids in the main Wadi Milaha section is documented 1 m above than in the coeval section WM2. This difference could have been caused by higher wave energy at WM 2 locality than in the main section causing the accretion of concentric layers on radial ooids (prevalence of local sedimentological variability on seawater chemistry parameters). However, the fact that this oolitic cycle C1 starts above a subaerial erosive surface and is followed by peloidal packstone typical of lagoonal conditions do speak for an environment on the upper ramp and not in open marine shoal settings. The wave-energy could be temporarily enhanced by the post-extinction lack of rims or shoals in the more open-marine settings (see the unreefing discussion above).

Regarding the oolitic assemblage in cycle C2, Ge et al. (2019) emphasized the poor preservation of nuclei and cortices of ooids, with frequent oomolds filled by coarse calcite spar. Borings and deformation are stated as other characteristics for the ooids in this interval. In our main Wadi Milaha section, ooids are micritized but not affected by oomoldic porosity and calcite spar replacement. Instead, the ooids are overall better preserved, highlighting the local effect of the dissolution features noted by Ge et al. (2019). Deformation of grains is also quite rare. These features, therefore, appear to be strictly local and not a key characteristic for the entire cycle. In cycle C2, the progressive decrease in size of the ooids could have been caused by the change in wave energy. Indeed, this cycle is characterized by a shift from high energy SMF with grainstones at the base to lower energy SMF with mainly packstones, packstones/wackestones or wackestones/mudstones and mudstones towards the top. Alternatively, a change in seawater chemistry parameters farther in time from the extinction event (e.g., change in water saturation state with respect to carbonate, in Mg/Ca ratio or in nutrient supply) could also explain these changes.

The 3–4 m thick part of C3 cycle presented by Ge et al. (2019) shows small micritic ooids, with quartz-bearing lithoclasts as nuclei. We consider these features as local, since the starting point of this cycle in our main Wadi Milaha section is instead characterized by a prevalence of partially recrystallized superficially coated grains, without significant quartz input. Peloids are abundant in these samples. Both Ge et al. (2018 and 2019) logged Wadi Milaha until their cycle C3 only. The main section presented in our study continues beyond this cycle C3 and indicates an evolution towards small micritized ooids, partially recrystallized. However, they are scattered in peloidal grainstones and do not show strong variability in origins of nuclei, irregular morphologies, deformation, break-up, etc. Partial dissolution of ooids outer laminae and preservation of the inner radial ones is advocated in Ge et al. (2019) to originate mixed fabrics in C2 and C3. This phenomenon was not observed in our samples. As for cycle C2, we could advocate a change in the previously mentioned seawater chemistry and sedimentological factors to motivate the small size of the coated grains, but also the development of thicker cortices around the nuclei. Comparison between cycles C1, C2 and C3 as originally described in Ge et al. (2018 and 2019) and the implemented description given in this study also includes the original mineralogy of ooids and superficially coated grains. In a later publication soon available, we will provide evidences on how they are probably calcitic in origin. This contradicts both the prediction of aragonite-calcite seas alternation as presented by Sandberg (1983) and Stanley and Hardie (1999) and the assumption in Ge et al. (2018 and 2019).

6. Conclusions

Analysis of the Wadi Milaha sections provided new insights into the geochemistry and sedimentology of the late Triassic-early Jurassic. The $\delta^{13}C_{carb}$ record presented herein shows a negative excursion for the mid-Norian, which could be however a local signal due to water restriction in this shallow setting. Across the Norian-Rhaetian Boundary (NRB), the $\delta^{13}C_{org}$ record is very stable and in agreement with the data of Kovács (2021). The NRB itself was well constrained due to findings of the conodonts *Epigondolella bidentata* and *Misikella posthernsteini* and the ammonoid *Neotibetites* sp.

The isotopic C and O curves retrieved from post-ETME beds constitute a robust, non-diagenetically overprinted record, although the late Triassic marshi CIE is lacking. We demonstrate the presence of a stratigraphic hiatus of unknown extent at the extinction level, supported by a clear erosional surface. This level displays a dramatic change in facies from pre-extinction coral-rich rudstones/floatstones to post-extinction less fossiliferous packstone/grainstones with high abundance of ooids. The TJB interval in Wadi Milaha section preserves the same transgressive trend as other Hettangian sections around the world. The features of this transgression can be linked to an abrupt demise of the carbonate factory at the ETME and motivate an extension of the "unreefing" model paradigma by Pálfy et al. (2021) into southern latitude platforms like the Arabic platform. Our focus on the coated grains deposited after the ETME produced new morphological classification. The coarsening-upward trend of oolitic cycles C1, C2 and C3 is confirmed only for cycle C1, while we addressed the poor preservation and deformation of ooids in cycle C2 as strictly local, as well as the micritic appearance of ooids and the siliciclastic input in cycle C3. We consider the extreme variability of post-extinction ooids a product of both water chemistry (redox conditions, nutrients supply, rate of dissolved carbon in marine water) and local sedimentological (wave energy) factors. In the light of these final considerations, further geochemical investigations at the ooids laminae scale are advocated to determine if either global water chemistry or sedimentological variables are predominant in the process of precipitation of such a morphological variety of post-ETME ooids. We will discuss these issues in a later publication.

CRediT authorship contribution statement

Ingrid Urban: Conceptualization, Methodology, Validation, Formal

analysis, Investigation, Resources, Data curation, Writing – original draft, Writing – review & editing, Visualization, Funding acquisition. **Isaline Demangel:** Formal analysis, Investigation, Writing – review & editing, Visualization. **Leopold Krystyn:** Formal analysis, Investigation, Writing – review & editing, Visualization. **Mikael Calner:** Writing – review & editing, Supervision. **Zsófia Kovács:** Investigation, Writing – review & editing. **Gerit Gradwohl:** Formal analysis, Investigation, Writing – review & editing, Visualization. **Simon Lernpeiss:** Formal analysis, Investigation, Writing – review & editing, Visualization. **Florian Maurer:** Formal analysis, Investigation, Writing – review & editing. **Sylvain Richoz:** Conceptualization, Methodology, Validation, Formal analysis, Investigation, Resources, Data curation, Writing – original draft, Writing – review & editing, Visualization, Supervision, Project administration, Funding acquisition.

Declaration of Competing Interest

The authors declare that they have no known competing financial interests or personal relationships that could have appeared to influence the work reported in this paper.

Data availability

Data used for this article are shared as supplement material.

Acknowledgements

This work was financially supported by the Crafoord Foundation (Crafoordska stiftelsen) [grant 2017 to Sylvain Richoz], the Royal Physiographic Society of Lund (Kungliga Fysiografiska Sällskapets i Lund) [grants 2018 and 2019 to Ingrid Urban] and the Austrian National Committee (Austrian Academy of Sciences) [IGCP: Project IGCP 572 and 630] for the fieldworks in 2015, 2018 and 2020 for SR, IU, ID, ZK, LK, SL, and GG.

Appendix A. Supplementary material

Supplementary data to this article can be found online at https://doi.org/10.1016/j.jaesx.2023.100138.

References

Ahlberg, A., Olsson, I., Šimkevičius, P., 2003. Triassic-Jurassic weathering and clay mineral dispersal in basement areas and sedimentary basins of southern Sweden. Sed. Geol. 161 (1–2), 15–29.

Al-Suwaidi, A.H., Steuber, T., Suarez, M.B., 2016. The Triassic-Jurassic boundary event from an equatorial carbonate platform (Ghalilah Formation, United Arab Emirates). J. Geol. Soc. Lond. 173 (6), 949–953.

Anderson, N.T., Cowan, C.A., Bergmann, K.D., 2020. A case for the growth of ancient ooids within the sediment pile. J. Sediment. Res. 90 (8), 843–854.

Bachan, A., van de Schootbrugge, B., Fiebig, J., McRoberts, C.A., Ciarapica, G., Payne, J. L., 2012. Carbon cycle dynamics following the end-Triassic mass extinction: constraints from paired $\delta^{13}C_{carb}$ and $\delta^{13}C_{org}$ records. Geochem. Geophys. Geosyst. 13 (9).

Bachan, A., van de Schootbrugge, B., Payne, J.L., 2014. The end-Triassic negative $\delta^{13}C$ excursion: a lithologic test. Palaeogeogr. Palaeoclimatol. Palaeoecol. 412, 177–186.

Bambach, R.K., Knoll, A.H., Sepkoski, J.J., 2002. Anatomical and ecological constraints on Phanerozoic animal diversity in the marine realm. Proc. Natl. Acad. Sci. 99 (10), 6854–6859.

Barattolo, F., De Castro, P., and Parente, M., 1994. Some remarks on the genera Palaeodasycladus (Pia, 1920) Pia, 1927 and Eodasycladus Cros and Lemoine, 1966 ex Granier and Deloffre, 1993 (Green Algae, Dasycladales). In Proceedings of the international symposium and field-meeting "Alpine Algae '93''. Beiträge zur Paläontologie (Vol. 19, pp. 1-11).

Bartolini, A., Guex, J., Spangenberg, J.E., Schoene, B., Taylor, D.G., Schaltegger, U., Atudorei, V., 2012. Disentangling the Hettangian carbon isotope record: Implications for the aftermath of the end-Triassic mass extinction. Geochem. Geophys. Geosyst. 13 (1), 1–11. https://doi.org/10.1029/2011GC003807.

Batchelor, M.T., Burne, R.V., Henry, B.I., Li, F., Paul, J., 2018. A biofilm and organomineralisation model for the growth and limiting size of ooids. Sci. Rep. 8 (1), 1–9.

Benton, M.J., 1995. Diversification and extinction in the history of life. Science 268 (5207), 52–58. https://doi.org/10.1126/science.7701342.

Berra, F., Angiolini, L., 2014. The evolution of the Tethys region throughout the Phanerozoic: A brief tectonic reconstruction.

Bhargava, O.N., Krystyn, L., Balini, M., Lein, R., Nicora, A., 2004. Revised litho- and sequence stratigraphy of the Spiti Triassic. Albertiana 30, 21–39.

Biehler, J., Chevalier, C., Ricateau, R., 1975. Geological map of the Musandam Peninsula, Oman. Directorate General of Petroleum and Minerals. Sultanate of Oman.

Brusatte, S.L., Benton, M.J., Ruta, M., Lloyd, G.T., 2008. Superiority, competition, and opportunism in the evolutionary radiation of dinosaurs. Science 321 (5895), 1485–1488.

Carozzi, A.V., 1957. Contribution à l'étude des propriétés géométriques des oolithes. L'exemple du Grand Lac Salé, Utah, USA. Bulletin de l'Institut national genevois 58, 3–52.

Chayes, F., 1954. The theory of thin-section analysis. J. Geol. 62 (1), 92–101.

Clapham, M.E., Payne, J.L., 2011. Acidification, anoxia, and extinction: A multiple logistic regression analysis of extinction selectivity during the Middle and Late Permian. Geology 39 (11), 1059–1062. https://doi.org/10.1130/g32230.1.

Clarkson, M.O., Richoz, S., Wood, R.A., Maurer, F., Krystyn, L., McGurty, D.J., Astratti, D., 2013. A new high-resolution $\delta^{13}C$ record for the Early Triassic: insights from the Arabian Platform. Gondw. Res. 24 (1), 233–242.

Dal Corso, J., Bernardi, M., Sun, Y., Song, H., Seyfullah, L. J., Preto, N., Gianolla, P., Ruffel, A., Kustacher, E., Roghi, G., Merico, a., Hohn, S., Schmidt, A. S., Marzoli, A., Newton, R. J., Wignall, P. B., and Benton, M. J., 2020. Extinction and dawn of the modern world in the Carnian (Late Triassic). Science Advances, 6(38), eaba0099.

Dal Corso, J., Marzoli, A., Tateo, F., Jenkyns, H.C., Bertrand, H., Youbi, N., Mahmoudi, A., Font, E., Buratti, N., Cirilli, S., 2014. The dawn of CAMP volcanism and its bearing on the end-Triassic carbon cycle disruption. J. Geol. Soc. Lond. 171, 153–164.

Davies, J.H.F.L., Marzoli, A., Bertrand, H., Youbi, N., Ernesto, M., Schaltegger, U., 2017. End-Triassic mass extinction started by intrusive CAMP activity. Nat. Commun. 8 (1), 1–8.

Davies, P.J., Bubela, B., Ferguson, J., 1978. The formation of ooids. Sedimentology 25 (5), 703–730.

Demangel, I., Howe, R., Gardin, S., Richoz, S., 2021. Eoconusphaera hallstattensis, new species, and review of the Rhaetian genus Eoconusphaera. J. Nannoplankton Res. 39–131.

Demangel, I., Kovács, Z., Richoz, S., Gardin, S., Krystyn, L., Baldermann, A., Piller, W.E., 2020. Development of Early Calcareous Nannoplankton in the Late Triassic Northern Calcareous Alps (Austria).

de Matos, J.E., 1997. Stratigraphy, Sedimentation and Oil Potential of the Lower Jurassic to Kimmeridgian of the United Arab Emirates; Outcrop and Subsurface Compared. University of Aberdeen. PhD thesis.

Diaz, M.R., Eberli, G.P., Blackwelder, P., Phillips, B., Swart, P.K., 2017. Microbially mediated organomineralization in the formation of ooids. Geology 45 (9), 771–774.

Diaz, M.R., Eberli, G.P., 2019. Decoding the mechanism of formation in marine ooids: a review. Earth Sci. Rev. 190, 536–556.

Diaz, M.R., Van Norstrand, J.D., Eberli, G.P., Piggot, A.M., Zhou, J., Klaus, J.S., 2014. Functional gene diversity of oolitic sands from Great Bahama Bank. Geobiology 12 (3), 231–249.

Duguid, S.M.A., Kurtis Kyser, T., James, N.P., Rankey, E.C., 2010. Microbes and ooids. J. Sediment. Res. 80, 236–251.

Dunham, R. J., 1962. Classification of carbonate rocks according to depositional textures.

Dupraz, C., Reid, R.P., Braissant, O., Decho, A.W., Norman, R.S., Visscher, P.T., 2009. Processes of carbonate precipitation in modern microbial mats. Earth Sci. Rev. 96 (3), 141–162.

Embry, A.F., Klovan, J.E., 1971. A late Devonian reef tract on northeastern Banks Island, NWT. Bull. Can. Petrol. Geol. 19 (4), 730–781.

Falkowski, P.G., Katz, M.E., Knoll, A.H., Quigg, A., Raven, J.A., Schofield, O., Taylor, F.J. R., 2004. The evolution of modern eukaryotic phytoplankton. Science 305 (5682), 354–360. https://doi.org/10.1126/science.1095964.

Felber, R., Weissert, H.J., Furrer, H., Bontognali, T.R., 2015. The Triassic-Jurassic boundary in the shallow-water marine carbonates from the western Northern Calcareous Alps (Austria). Swiss J. Geosci. 108 (2), 213–224.

Flügel, E., 2010. Microfacies of Carbonate Rocks, Analysis. Springer-Verlag, Berlin, Interpretation and Application, p. 976.

Folk, R.L., Leo Lynch, F., 2001. Organic matter, putative nannobacteria and the formation of ooids and hardgrounds. Sedimentology 48 (2), 215–229.

Galbrun, B., Boulila, S., Krystyn, L., Richoz, S., Gardin, S., Bartolini, A., Maslo, M., 2020. " Short" or" long" Rhaetian? Astronomical calibration of Austrian key sections. Global Planet. Change 192, 103253.

Galehouse, J.S., 1971. Point counting. In: Carver, R.E. (Ed.), Procedures in Sedimentary Petrology: New York. John Wiley and Sons, pp. 385–407.

Galli, M.T., Jadoul, F., Bernasconi, S.M., Cirilli, S., Weissert, H., 2007. Stratigraphy and palaeoenvironmental analysis of the Triassic-Jurassic transition in the western Southern Alps (Northern Italy). Palaeogeogr. Palaeoclimatol. Palaeoecol. 244 (1–4), 52–70.

Ge, Y., 2021. Decoupled $\delta^{13}C_{carb}$ and $\delta^{13}C_{org}$ records at Triassic-Jurassic boundary interval in eastern Tethys: Environmental implications for spatially different global response. Geosci. Front. 12 (4), 101146.

Ge, Y., Al-Suwaidi, A.H., Shi, M., Li, Q., Morad, S., Steuber, T., 2019. Short-term variation of ooid mineralogy in the Triassic-Jurassic boundary interval and its environmental implications: Evidence from the equatorial Ghalilah Formation, United Arab Emirates. Global Planet. Change 182, 103006.

Ge, Y., Shi, M., Steuber, T., Al-Suwaidi, A.H., Suarez, M.B., 2018. Environmental change during the Triassic-Jurassic boundary interval of an equatorial carbonate platform:

sedimentology and chemostratigraphy of the Ghalilah Formation, United Arab Emirates. Palaeogeogr. Palaeoclimatol. Palaeoecol. 502, 86–103.
Gerdes, G., Dunajtschik-Piewak, K., Riege, H., Taher, A.G., Krumbein, W.E., Reineck, H.-E., 1994. Structural diversity of biogenic carbonate particles in microbial mats. Sedimentology 41, 1273–1294.
Glennie, K.W., 2005. The Geology of the Oman Mountains, an outline of their origin. Scientific Press Beaconsfield, Bucks, UK.
Glennie, K.W., Boeuf, M.G.A., Huges-Clarke, M.W., Moody-Stuart, M., Pilaar, W.F.H., Reinhardt, B.M., 1974. Geology of the Oman Mountains. The Hague, Martinus Nijhoff, Verhandelingen Koninklijk Nederlands Geologie en Mijnbouw Genootschap, 31:1–423.
Greene, S.E., Bottjer, D.J., Corsetti, F.A., Berelson, W.M., Zonneveld, J.P., 2012a. A subseafloor carbonate factory across the Triassic-Jurassic transition. Geology 40 (11), 1043–1046.
Greene, S.E., Martindale, R.C., Ritterbush, K.A., Bottjer, D.J., Corsetti, F.A., Berelson, W. M., 2012b. Recognising ocean acidification in deep time: an evaluation of the evidence for acidification across the Triassic-Jurassic boundary. Earth Sci. Rev. 113 (1–2), 72–93.
Groves, J.R., Calner, M., 2004. Lower Triassic oolites in Tethys: a sedimentologic response to the end-Permian mass extinction. Geological Society of America, annual meeting, Denver, 7-10 Nov. 2004, Abstracts with Programs 36 (5), p. 336.
Hallam, A., Wignall, P.B., 1999. Mass extinctions and sea-level changes. Earth Sci. Rev. 48, 217–250. https://doi.org/10.1016/S0012-8252(99)00055-0.
Haq, B.U., 2018. Triassic eustatic variations reexamined. Gsa Today, 28(12), 4-9.
Haq, B.U., Al-Qahtani, A.M., 2005. Phanerozoic cycles of sea-level change on the Arabian Platform. GeoArabia 10 (2), 127–160.
Hautmann, M., 2004. Effect of the end-Triassic CO_2 maximum on carbonate sedimentation and marine mass extinction. Facies 50, 257–261.
Hautmann, M., Benton, M.J., Tomašových, A., 2008. Catastrophic ocean acidification at the Triassic-Jurassic boundary. Neues Jahrb. Geol. Palaontol. Abh. 249, 119–127.
Heydari, E., Moore, C.H., 1994. Paleoceanographic and paleoclimatic controls on ooid mineralogy of the Smackover Formation, Mississippi salt basin; implications for Late Jurassic seawater composition. J. Sediment. Res. 64 (1a), 101–114.
Heimdal, T.H., Jones, M.T., Svensen, H.H., 2020. Thermogenic carbon release from the Central Atlantic magmatic province caused major end-Triassic carbon cycle perturbations. Proc. Natl. Acad. Sci. 117 (22), 11968–11974.
Hesselbo, S.P., McRoberts, C.A., Pálfy, J., 2007. Triassic-Jurassic boundary events: problems, progress, possibilities. Palaeogeogr., Palaeoclimatol. Palaeoecol. 244, 1–10. https://doi.org/10.1016/j.palaeo.2006.06.020.
Hesselbo, S.P., Robinson, S.A., Surlyk, F., Piasecki, S., 2002. Terrestrial and marine extinction at the Triassic-Jurassic boundary synchronized with major carbon-cycle perturbation: a link to initiation of massive volcanism? Geology 30 (3), 251–254. https://doi.org/10.1130/0091-7613(2002)030<0251:TAMEAT>2.0.CO;2.
Hillebrandt, A.V., Krystyn, L., Kürschner, W.M., Bonis, N.R., Ruhl, M., Richoz, S., Schobben, M.A.N., Urlichs, M., Bown, P.R., Kment, K., McRoberts, C.A., Simms, M., Tomäsových, A., 2013. The global stratotype sections and point (GSSP) for the base of the Jurassic System at Kuhjoch (Karwendel Mountains, Northern Calcareous Alps, Tyrol, Austria). Episodes 36 (3), 162–198.
Hudson, R.G.S., 1960. The Permian and Trias of the Oman Peninsula, Arabia. Geol. Mag. 97, 299–308.
Hudson, R.G.S., Jefferies, R.P.S., 1961. Upper Triassic brachiopods and lamellibranchs from the Oman Peninsula, Arabia. Paleontology 4, 1–41.
Hönig, M.R., John, C.M., Manning, C., 2017. Development of an equatorial carbonate platform across the Triassic-Jurassic boundary and links to global palaeoenvironmental changes (Musandam Peninsula, UAE/Oman). Gondw. Res. 45, 100–117.
Jost, A.B., Bachan, A., van de Schootbrugge, B., Brown, S.T., DePaolo, D.J., Payne, J.L., 2017. Additive effects of acidification and mineralogy on calcium isotopes in Triassic/Jurassic boundary limestones. Geochem. Geophys. Geosyst. 18 (1), 113–124.
Issautier, B., Le Nindre, Y-M., Hooker, N., Reid, C., Memesh, A. and Dini, S., 2019. Depositional environments, age, and sequence stratigraphy of the Minjur Formation in outcrop and near subsurface—Central Saudi Arabia. In H. R. AlAnzi, R. A. Rahmani, R. J. Steel and O. M. Soliman, eds., Siliciclastic reservoirs of the Arabian plate: AAPG Memoir 116, p. 141–184.
Kaiho, K., Tanaka, D., Richoz, S., Jones, D.S., Saito, R., Kameyama, D., Ikeds, M., Takahashi, S., Aftabuzzuman, M.d., Fujibayashi, M., 2022. Volcanic temperature changes modulated volatile release and climate fluctuations at the end-Triassic mass extinction. Earth Planet. Sci. Lett. 579, 117364 https://doi.org/10.1016/j.epsl.2021.117364.
Kent, D.V., Olsen, P.E., Muttoni, G., 2017. Astrochronostratigraphic polarity time scale (APTS) for the Late Triassic and Early Jurassic from continental sediments and correlation with standard marine stages. Earth Sci. Rev. 166, 153–180.
Kiessling, W., 2010. Reef expansion during the Triassic: Spread of photosymbiosis balancing climatic cooling. Palaeogeogr. Palaeoclimatol. Palaeoecol. 290 (1–4), 11–19.
Kiessling, W., Aberhan, M., Brenneis, B., Wagner, P.J., 2007. Extinction trajectories of benthic organisms across the Triassic-Jurassic boundary. Palaeogeogr. Palaeoclimatol. Palaeoecol. 244 (1–4), 201–222.
Knobbe, T.K., Schaller, M.F., 2018. A tight coupling between atmospheric pCO2 and sea-surface temperature in the Late Triassic. Geology 46 (1), 43–46.
Knoll, A.H., Bambach, R.K., Payne, J.L., Pruss, S., Fischer, W.W., 2007. Paleophysiology and end-Permian mass extinction. Earth Planet. Sci. Lett. 256 (3–4), 295–313. https://doi.org/10.1016/j.epsl.2007.02.018.
Korte, C., Kozur, H.W., Veizer, J., 2005. $\delta^{13}C$ and $\delta^{18}O$ values of Triassic brachiopods and carbonate rocks as proxies for coeval seawater and palaeotemperature. Palaeogeogr. Palaeoclimatol. Palaeoecol. 226 (3–4), 287–306. https://doi.org/10.1016/j.palaeo.2005.05.018.
Kovács, Z., 2021. The origin of pelagic calcification and its influence on seawater chemistry. PhD Thesis, 294 p. Graz University.
Kovács, Z., Demangel, I., Richoz, S., Hippler, D., Baldermann, A., Krystyn, L., 2020. New constraints on the evolution of $^{87}Sr/^{86}Sr$ of seawater during the Upper Triassic. Global Planetary Change 192, 103255.
Kovács, Z., Demangel, I., Schmitt, A.-D., Gangloff, S., Baldermann, A., Hippler, D., Krystyn, L., and Richoz, S., 2022. The calcium isotope ($\delta^{44}/^{40}Ca$) record through environmental changes: Insights from the Late Triassic. Geochemistry, Geophysics, Geosystems 23, e2022GC010405. https://doi.org/10.1029/2022GC010405.
Krystyn, L., Bouquerel, H., Kuerschner, W., Richoz, S., Gallet, Y., 2007a. Proposal for a candidate GSSP for the base of the Rhaetian stage. In: Lucas, S.G., Spielmann, J.A. (Eds.), The Global Triassic. 41. New Mexico Museum of Natural History and Science Bulletin, pp. 189–199.
Krystyn, L., Richoz, S., Gallet, Y., Bouquerel, H., Kürschner, W.M., Spötl, C., 2007b. Updated bio-and magnetostratigraphy from Steinbergkogel (Austria), candidate GSSP for the base of the Rhaetian stage. Albertiana 36, 164–172.
Kump, L. R., and Hine, A. C., 1986. Ooids as sea-level indicators. In Sea-Level Research (pp. 175-193). Springer, Dordrecht.
Li, F., Gong, Q., Burne, R.V., Tang, H., Su, C., Zeng, K., Zhang, Y., Tan, X., 2019. Ooid factories operating under hothouse conditions in the earliest Triassic of South China. Global Planet. Change 172, 336–354.
Li, F., Yan, J., Algeo, T., Wu, X., 2013. Paleoceanographic conditions following the end-Permian mass extinction recorded by giant ooids (Moyang, South China). Global Planet. Change 105, 102–120.
Li, F., Yan, J., Chen, Z.Q., Ogg, J.G., Tian, L., Korngreen, D., Liu, K., Ma, Z., Woods, A.D., 2015. Global oolite deposits across the Permian-Triassic boundary: a synthesis and implications for palaeoceanography immediately after the end-Permian biocrisis. Earth Sci. Rev. 149, 163–180.
Li, F., Yan, J., Burne, R.V., Chen, Z.Q., Algeo, T.J., Zhang, W., Tian, L., Gan, Y., Liu, K., Xie, S., 2017. Paleo-seawater REE compositions and microbial signatures preserved in laminae of Lower Triassic ooids. Palaeogeogr. Palaeoclimatol. Palaeoecol. 486, 96–107.
Lindström, S., Callegaro, S., Davies, J., Tegner, C., Van De Schootbrugge, B., Pedersen, G. K., 2021. Tracing volcanic emissions from the Central Atlantic Magmatic Province in the sedimentary record. Earth Sci. Rev. 212, 103444 https://doi.org/10.1016/j.earscirev.2020.103444.
Lindström, S., Pedersen, G.K., Van De Schootbrugge, B., Hansen, K.H., Kuhlmann, N., Thein, J., Johansson, L., Petersen, H.I., Alwmark, C., Dybkjær, K., Weibel, R., Erlström, M., Nielsen, L.H., Oschmann, W., Tegner, C., 2015. Intense and widespread seismicity during the end-Triassic mass extinction due to emplacement of a large igneous province. Geology 43 (5), 387–390.
Lindström, S., van de Schootbrugge, B., Dybkjær, K., Pedersen, G.K., Fiebig, J., Nielsen, L. H., Richoz, S., 2012. No causal link between terrestrial ecosystem change and methane release during the end-Triassic mass-extinction. Geology 40, 531–534.
Lindström, S., van de Schootbrugge, B., Hansen, K.H., Pedersen, G.K., Alsen, P., Thibault, N., Dybkjær, K., Bierrum, C.J., Nielsen, L.H., 2017. A new correlation of Triassic-Jurassic boundary successions in NW Europe, Nevada and Peru, and the Central Atlantic Magmatic Province: A time-line for the end-Triassic mass extinction. Palaeogeogr. Palaeoclimatol. Palaeoecol. 478, 80–102.
Lohmann, K.C., 1988. Geochemical patterns of meteoric diagenetic systems and their application to studies of paleokarst. In: James, N.P., Choquette, P.W. (Eds.), Paleokarst. Springer-Verlag, Berlin, pp. 50–80.
Mander, L., Twitchett, R.J., Benton, M.J., 2008. Palaeoecology of the Late Triassic extinction event in the SW UK. J. Geol. Soc. Lond. 165, 319–332.
Marcoux, J., Baud, A., Ricou, L.E., Gaetani, M., Krystyn, L., Bellion, Y., Guiraud, R., Besse, J., Gallet, Y., Jaillard, E., Moreau, C., Theveniaut, H., 1993. Late Norian (215–212 Ma). In: Dercourt, J., Ricou, L.E., Vrielynck, B. (Eds.), Atlas Tethys Palaeoenvironment Maps Explanatory Notices. Paris, Gauthiers-Villars, pp. 35–53.
Maron, M., Rigo, M., Bertinelli, A., Katz, M.E., Godfrey, L., Zaffani, M., Muttoni, G., 2015. Magnetostratigraphy, biostratigraphy, and chemostratigraphy of the Pignola-Abriola section: New constraints for the Norian-Rhaetian boundary. Bulletin 127 (7–8), 962–974.
Marzoli, A., Callegaro, S., Dal Corso, J., Davies, J.H., Chiaradia, M., Youbi, N., Bertrand, H., Reisberg, L., Merle, R., Jourdan, F., 2018. The Central Atlantic magmatic province (CAMP): a review. In: The Late Triassic World. Springer, Cham, pp. 91–125.
Marzoli, A., Renne, P.R., Piccirillo, E.M., Ernesto, M., Bellieni, G., Min, A.D., 1999. Extensive 200-million-year-old continental flood basalts of the central atlantic magmatic province. Science 284 (5414), 616–618. https://doi.org/10.1126/science.284.5414.616.
Maurer, F., Krystyn, L., Martini, R., McRoberts, C., Rettori, R. and Hofmann, P., 2015. Towards a refined Arabian Plate Triassic stratigraphy: insights from the Musandam Peninsula (UAE & Oman). EAGE 5th Arabian Plate workshop, 8-11 February 2015, Kuwait.
Maurer, F., Martini, R., Rettori, R., Hillgärtner, H., Cirilli, S., 2009. The geology of Khuff outcrop analogues in the Musandam Peninsula, United Arab Emirates and Oman. GeoArabia 14 (3), 125–158.
Maurer, F., Rettori, R., Martini, R., 2008. Triassic stratigraphy, facies and evolution of the Arabian shelf in the northern United Arab Emirates. Int. J. Earth Sci. 97 (4), 765–784.
McElwain, J.C., Beerling, D.J., Woodward, F.I., 1999. Fossil plants and global warming at the Triassic-Jurassic boundary. Science 285 (5432), 1386–1390.

McRoberts, C.A., Krystyn, L., Shea, A., 2008. Rhaetian (Late Triassic) Monotis (Bivalvia: Pectinoida) from the eastern Northern Calcareous Alps (Austria) and the end-Norian crisis in pelagic faunas. Palaeontology 51 (3), 721–735.
McRoberts, C.A., Newton, C.R., 1995. Selective extinction among end-Triassic European bivalves. Geology 23 (2), 102–104.
Muttoni, G., Kent, D.V., Olsen, P.E., Stefano, P.D., Lowrie, W., Bernasconi, S.M., Hernández, F.M., 2004. Tethyan magnetostratigraphy from Pizzo Mondello (Sicily) and correlation to the Late Triassic Newark astrochronological polarity time scale. Geol. Soc. Am. Bull. 116 (9–10), 1043–1058.
Muttoni, G., Mazza, M., Mosher, D., Katz, M.E., Kent, D.V., Balini, M., 2014. A Middle-Late Triassic (Ladinian–Rhaetian) carbon and oxygen isotope record from the Tethyan Ocean. Palaeogeogr. Palaeoclimatol. Palaeoecol. 399, 246–259. https://doi.org/10.1016/j.palaeo.2014.01.018.
Obermaier, M., Aigner, T., Forke, H.C., 2012. Facies, sequence stratigraphy and reservoir/seal potential of a Jilh Formation outcrop equivalent (Wadi Sahtan, Triassic, Upper Mahil Member, Sultanate of Oman). GeoArabia 17 (3), 85–128.
Olsen, P.E., Kent, D.V., Whiteside, J.H., 2010. Implications of the Newark Supergroup-based astrochronology and geomagnetic polarity time scale (Newark-APTS) for the tempo and mode of the early diversification of the Dinosauria. Earth Environ. Sci. Trans. R. Soc. Edinb. 101 (3–4), 201–229.
Onoue, T., Yamashita, K., Fukuda, C., Soda, K., Tomimatsu, Y., Abate, B., Rigo, M., 2018. Sr isotope variations in the Upper Triassic succession at Pizzo Mondello, Sicily: Constraints on the timing of the Cimmerian Orogeny. Palaeogeogr. Palaeoclimatol. Palaeoecol. 499, 131–137.
Onoue, T., Zonneveld, J.P., Orchard, M.J., Yamashita, M., Yamashita, K., Sato, H., Kusaka, S., 2016. Paleoenvironmental changes across the Carnian/Norian boundary in the Black Bear Ridge section, British Columbia, Canada. Palaeogeogr. Palaeoclimatol. Palaeoecol. 441, 721–733.
Opdyke, B.N., Wilkinson, B.H., 1990. Paleolatitude distribution of Phanerozoic marine ooids and cements. Palaeogeogr. Palaeoclimatol. Palaeoecol. 78 (1–2), 135–148.
Pálfy, J., Kovács, Z., Demény, A., Vallner, Z., 2021. End-Triassic crisis and "unreefing" led to the demise of the Dachstein carbonate platform: A revised model and evidence from the Transdanubian Range, Hungary. Global Planet. Change 199, 103428.
Price, G.D., 1999. The evidence and implications of polar ice during the Mesozoic. Earth Sci. Rev. 48 (3), 183–210. https://doi.org/10.1016/s0012-8252(99)00048-3.
Rankey, E.C., Reeder, S.L., 2009. Holocene ooids of Aitutaki Atoll, Cook Islands. South Pacific. Geology 37 (11), 971–974.
Reijmer, J.J., Ten Kate, W.G.H.Z., Sprenger, A., Schlager, W., 1991. Calciturbidite composition related to exposure and flooding of a carbonate platform (Triassic, Eastern Alps). Sedimentology 38 (6), 1059–1074.
Richoz, S., Baud, A., Beauchamp, B., Grasby, S., Henderson, C., Krystyn, L., 2014. Khuff margin: slope to oceanic deposits (Permian-Triassic Allochthons and Exotics, Oman). In: Poeppelreiter,, . (Ed.), The Khuff Formation. New perspective. EAGE Publications. Houten, The Nederlands, pp. 55–76. ISBN 978-90-73834-42-2.
Richoz, S., Krystyn, L., Spötl, C., and Kürschner, W. M., 2008. Building an Upper Triassic carbon isotope reference curve. na.
Richoz, S., Krystyn, L., Baud, A., Brandner, R., Horacek, M., Mohtat-Aghai, P., 2010. Permian-Triassic boundary interval in the Middle East (Iran and N. Oman): progressive environmental change from detailed carbonate carbon isotope marine curve and sedimentary evolution. J. Asian Earth Sci. 39, 236–253. https://doi.org/10.1016/j.jseaes.2009.12.014.
Richoz, S., Krystyn, L., von Hillebrandt, A., Martindale, R., 2012. End-Triassic crisis events recorded in platform and basin of the Austrian Alps. The Triassic/Jurassic and Norian/Rhaetian GSSPs. J. Alpine Geol. 54, 323–377.
Richoz, S. and Krystyn, L., 2015. The Upper Triassic events recorded in platform and basin of the Austrian Alps. The Triassic/Jurassic GSSP and Norian/Rhaetian GSSP candidate. B. der Geol. Bundesansltalt 111, 75-136, Wien, Austria.
Rigo, M., Bertinelli, A., Concheri, G., Gattolin, G., Godfrey, L., Katz, M.E., Maron, M., Mietto, P., Muttoni, G., Sprovieri, M., Stellin, F., Zaffani, M., 2016. The Pignola-Abriola section (southern Apennines, Italy): a new GSSP candidate for the base of the Rhaetian Stage. Lethaia 49 (3), 287–306.
Rigo, M., Onoue, T., Tanner, L.H., Lucas, S.G., Godfrey, L., Katz, M.E., Zaffani, M., Grice, K., Cesar, J., Yamashita, D., Maron, M., Tackett, L.S., Campbell, H., Tateo, F., Concheri, G., Agnini, C., Chiari, M., Bertinelli, A., 2020. The Late Triassic Extinction at the Norian/Rhaetian boundary: Biotic evidence and geochemical signature. Earth Sci. Rev. 204, 103180 https://doi.org/10.1016/j.earscirev.2020.103180.
Roduit, N. JMicroVision: Image analysis toolbox for measuring and quantifying components of high-definition images. Version 1.3.1. https://jmicrovision.github.io (accessed 18 October 2022).
Roduit, N., 2007. JMicroVision: un logiciel d'analyse d'images pétrographiques polyvalent. University of Geneva. Doctoral dissertation,.
Ruhl, M., Hesselbo, S.P., Al-Suwaidi, A., Jenkyns, H.C., Damborenea, S.E., Manceñido, M.O., Storm, M., Mather, T.A., Riccardi, A.C., 2020. On the onset of Central Atlantic Magmatic Province (CAMP) volcanism and environmental and carbon-cycle change at the Triassic-Jurassic transition (Neuquén Basin, Argentina). Earth Sci. Rev. 103229 https://doi.org/10.1016/j.earscirev.2020.103229.
Ruhl, M., Kürschner, W.M., Krystyn, L., 2009. Triassic-Jurassic organic carbon isotope stratigraphy of key sections in the western Tethys realm (Austria). Earth Planet. Sci. Lett. 281 (3–4), 169–187.
Sandberg, P., 1983. An oscillating trend in Phanerozoic non-skeletal carbonate mineralogy. Nature 305, 19–22. https://doi.org/10.1038/305019a0.
Searle, M.P., 1988. Structure of the Musandam culmination (Sultanate of Oman and United Arab Emirates) and the Straits of Hormuz syntaxis. J. Geol. Soc. Lond. 145, 831–845.
Searle, M.P., Cherry, A.G., Ali, M.Y., Cooper, D.J., 2014. Tectonics of the Musandam Peninsula and northern Oman Mountains: From ophiolite obduction to continental collision. GeoArabia 19 (2), 135–174.
Senowbari-Daryan, B., Maurer, F., 2008. Upper Triassic (Norian) hypercalcified sponges from the Musandam Peninsula (United Arab Emirates and Oman). Facies 54, 433–460.
Sharland, P.R., Archer, R., Casey, D.M., Davies, R.B., Hall, S.H., Heward, A.P., Horbury, A.D., and Simmons, M.D., 2001. Sequence stratigraphy of the Arabian Plate. GeoArabia special Publication 2, Gulf PetroLink. Bahrain 2 (37), 1–371.
Shen, J., Yin, R., Zhang, S., Algeo, T.J., Bottjer, D.J., Yu, J., Xu, G., Penman, D., Wang, Y., Li, L., Shi, X., Planavski, N.J., Feng, Q., Xie, S., 2022. Intensified continental chemical weathering and carbon-cycle perturbations linked to volcanism during the Triassic-Jurassic transition. Nat. Commun. 13 (1), 1–10.
Simone, L., 1980. Ooids: a review. Earth Sci. Rev. 16, 319–355.
Stanley, S.M., Hardie, L.A., 1999. Hypercalcification: paleontology links plate tectonics and geochemistry to sedimentology. GSA Today 9, 1–7.
Stewart, S.A., 2016. Structural geology of the Rub'Al-Khali Basin, Saudi Arabia. Tectonics 35 (10), 2417–2438.
Sumner, D.Y., Grotzinger, J.P., 1993. Numerical modeling of ooid size and the problem of Neoproterozoic giant ooids. J. Sediment. Res. 63 (5), 974–982.
Sun, Y.D., Orchard, M.J., Kocsis, Á.T., Joachimski, M.M., 2020. Carnian-Norian (Late Triassic) climate change: Evidence from conodont oxygen isotope thermometry with implications for reef development and Wrangellian tectonics. Earth Planet. Sci. Lett. 534, 116082.
Szabo, F., Keradpir, A., 1978. Permian and Triassic stratigraphy Zagros Basin, Southwest Iran. J. Petrol. Geol. 1 (2), 57–82. https://doi.org/10.1111/j.1747-5457.1978.tb00611.x.
Tanner, L.H., Lucas, S.G., 2015. The Triassic-Jurassic strata of the Newark Basin, USA: a complete and accurate astronomically-tuned timescale. Stratigraphy 12 (1), 47–65.
Trower, E.J., Cantine, M.D., Gomes, M.L., Grotzinger, J.P., Knoll, A.H., Lamb, M.P., Lingappa, U., O'Reilly, S.S., Present, T.M., Stein, N., Strauss, J.V., Fischer, W.W., 2018. Active ooid growth driven by sediment transport in a high-energy shoal, Little Ambergris Cay, Turks and Caicos Islands. J. Sediment. Res. 88 (9), 1132–1151.
Van de Schootbrugge, B., Van Der Weijst, C.M.H., Hollaar, T.P., Vecoli, M., Strother, P.K., Kuhlmann, N., Thein, J., Visscher, H., van Konijnenburg-van Cittert, H., Schobben, M.A.N., Sluijs, A., Lindström, S., 2020. Catastrophic soil loss associated with end-Triassic deforestation. Earth Sci. Rev. 210, 103332.
Weems, R.E., Tanner, L.H., Lucas, S.G., 2016. Synthesis and revision of the lithostratigraphic groups and formations in the Upper Permian? –Lower Jurassic Newark Supergroup of eastern North America. Stratigraphy 13 (2), 111–153.
Williford, K.H., Ward, P.D., Garrison, G.H., Buick, R., 2007. An extended organic carbon-isotope record across the Triassic-Jurassic boundary in the Queen Charlotte Islands, British Columbia, Canada. Palaeogeogr. Palaeoclimatol. Palaeoecol. 244 (1–4), 290–296. https://doi.org/10.1016/j.palaeo.2006.06.032.
Wilson, J.L., 1975. Carbonate facies in geologic history. 471 pp., Berlin (Springer).
Wotzlaw, J.-F., Guex, J., Bartolini, A., Gallet, Y., Krystyn, L., McRoberts, C.A., Taylor, D., Schoene, B., Schaltegger, U., 2014. Towards accurate numerical calibration of the late Triassic: high-precision U-Pb geochronology constraints on the duration of the Rhaetian. Geology 42, 571–574.
Wright, V.P., 1992. A revised classification of limestones. Sed. Geol. 76 (3–4), 177–185.
Zaffani, M., Agnini, C., Concheri, G., Godfrey, L., Katz, M., Maron, M., Rigo, M., 2017. The Norian "chaotic carbon interval": new clues from the $\delta^{13}C_{org}$ record of the Lagonegro Basin (southern Italy). Geosphere 13 (4), 1–16. https://doi.org/10.1130/GES01459.1.
Zaffani, M., Jadoul, F., Rigo, M., 2018. A new Rhaetian δ13Corg record: Carbon cycle disturbances, volcanism, End-Triassic mass Extinction (ETE). Earth-Sci. Rev. 178, 92–104. https://doi.org/10.1016/j.earscirev.2018.01.004.
Ziegler, M.A., 2001. Late Permian to Holocene paleofacies evolution of the Arabian Plate and its hydrocarbon occurrences. GeoArabia 6, 445–504.
Pierre, A., 2006. Un analogue de terrain pour les rampes oolitiques anciennes. Un affleurement continu à l'eéchelle de la sismique (falaises jurassiques d'Amellago, Haut Atlas, Maroc). Université de Bourgogne (PhD Thesis).
Thierry, J. and Barrier, E., 2000. Middle Toarcian. In: Dercourt, J., Gaetani, M., Vrielynck, B., Barrier, E., Biju-Duval, B., Brunet, M.F., Cadet, J.-P., Crasquin, S., Sandulescu, M. (Eds.), Atlas Peri-tethys, Palaeogeographical Maps (Commission de la carte géologique du monde: Paris).

Ingrid Urban is a carbonate sedimentology and geochemistry specialist. She studied geology in Padova (Italy) and Helsinki (Finland). She got her MSc degree in 2017 and she is now a PhD student at Lund University (Sweden). Her project focuses in petrographical and geochemical characterization of ooids deposited in the early aftermath of mass extinction events.

Sylvain Richoz studied geology and geochemistry at Lausanne University (Switzerland) and obtained there his PhD in 2004 on sedimentology and stratigraphy of the Permian-Triassic Boundary and the following recovery time interval in Oman, Turkey and Iran. After several positions at Vienna, Frankfurt and Graz Universities, he is since March 2017 senior lecturer for sedimentology at Lund University. His main focuses are Mesozoic mass-extinctions, carbonate deposition, the Mesozoic plankton evolution, the interactions between life evolution, climate and ocean chemistry during the Upper Permian to Lower Jurassic time. He is a specialist of the Tethys Realm.

Isaline Demangel is a calcareous nannoplankton specialist. She studied geology at Angers, Lille and Bochum and defended her PhD in March 2022 at Graz University on "The emergence of pelagic calcification and its influence on seawater chemistry in the Upper Triassic". She is now a Post-Doc at Lund University, working on Mesozoic phytoplankton.

Zsófia Kovács is a sedimentary geochemist. She studied geology in Budapest and Erlangen and defended her PhD in April 2021 at Graz University on "Multi-proxy characterization of the influence of the rising pelagic calcification on seawater chemistry". She is now working in quality control of medical research instruments.

Leopold Krystyn is a paleontologist, specialist in Triassic ammonoids, conodonts and pelagic bivalves with special emphasis of the refinement of the Global Time Scale. Other research interests are sequence stratigraphy and palaeobiogeography of the Triassic Tethys as well as the sedimentary history of its margins. He was a professor for Paleontology at Vienna University until 2011.

Gerit Gradwohl studied geology at Graz University where he got his Master of Science in 2020. After that, he worked on the landscape evolution of the Alps as a PhD student and is now working as a geotechnical engineer.

Simon Lernpeiss studied geology at Graz University. He is the owner of the enterprise 3D Druck Graz.

Florian Maurer is carbonate geology specialist at TotalEnergies working on Middle East and Brazil pre-salt carbonate assets. Previously he was exploration & reservoir geologist at Maersk Oil working on North Sea, Middle East and North Africa regions. Before joining the industry, Florian was Assistant Professor of Geology at the Petroleum Institute (Abu Dhabi) where he also carried out fieldwork in the Musandam Peninsula. Florian earned an MSc degree from Vienna University in 1999 and a PhD degree from Free University Amsterdam in 2003 for research on Middle Triassic carbonate platforms and basins in the Southern Alps of Italy.

Mikael Calner is a sedimentologist and stratigrapher with long-time interest in carbonate rocks as archive for environmental changes in past oceans. He has a particular interest in global change and in the impact of global climate and biodiversity change on carbonate platforms, including the deposition of time-specific facies related to minor and major extinction events.